Geophysical Journal International

Geophys. J. Int. (2012) **188,** 819–849

doi: 10.1111/j.1365-246X.2011.05313.x

3-D crustal structure along the North Anatolian Fault Zone in north-central Anatolia revealed by local earthquake tomography

Seda Yolsal-Çevikbilen,[1] C. Berk Biryol,[2] Susan Beck,[2] George Zandt,[2] Tuncay Taymaz,[1] Hande E. Adıyaman[2] and A. Arda Özacar[3]

[1] *Department of Geophysical Engineering, the Faculty of Mines, Istanbul Technical University, Maslak* TR-34469, *Istanbul, Turkey.*
E-mail: yolsalse@itu.edu.tr
[2] *Department of Geosciences, University of Arizona, Tucson, AZ* 85721, *USA*
[3] *Department of Geological Engineering, Middle East Technical University, İnönü Bulvarı,* 06531 *Ankara, Turkey*

Accepted 2011 November 21. Received 2011 November 21; in original form 2010 September 13

SUMMARY

3-D *P*-wave velocity structure and V_p/V_s variations in the crust along the North Anatolian Fault Zone (NAFZ) in north-central Anatolia were investigated by the inversion of local *P*- and *S*-wave traveltimes, to gain a better understanding of the seismological characteristics of the region. The 3-D local earthquake tomography inversions included 5444 *P*- and 3200 *S*-wave readings obtained from 168 well-located earthquakes between 2006 January and 2008 May. Dense ray coverage yields good resolution, particularly in the central part of the study area. The 3-D V_p and V_p/V_s tomographic images reveal clear correlations with both the surface geology and significant tectonic units in the region. We observed the lower limit of the seismogenic zone for north-central Anatolia at 15 km depth. Final earthquake locations display a distributed pattern throughout the study area, with most of the earthquakes occurring on the major splays of the NAFZ, rather than its master strand. We identify three major high-velocity blocks in the mid-crust separated by the İzmir-Ankara-Erzincan Suture and interpret these blocks to be continental basement fragments that were accreted onto the margin following the closure of Neo-Tethyan Ocean. These basement blocks may have in part influenced the rupture propagations of the historical 1939, 1942 and 1943 earthquakes. In addition, large variations in the V_p/V_s ratio in the mid-crust were observed and have been correlated with the varying fluid contents of the existing lithologies and related tectonic structures.

Key words: Seismicity and tectonics; Body waves; Seismic tomography; Continental tectonics: strike-slip and transform; Crustal structure.

1 INTRODUCTION

In this study we investigate the 3-D crustal structure along the North Anatolian Fault Zone (NAFZ) in northern-central Anatolia. It is a seismically active dextral strike-slip fault zone extending for about 1500 km from Karlıova in eastern Turkey to the Gulf of Saros in the Aegean Sea (Fig. 1a). Active tectonics of the North Central Anatolian region are governed by the complex collision of the Arabian, African and Eurasian plates and the resulting westward extrusion of Anatolian Plate between the right-lateral NAFZ and the left-lateral East Anatolian Fault Zone (EAFZ, McKenzie 1972; Şengör 1979; Şengör *et al.* 1985; Dewey *et al.* 1986; Taymaz 1996; Taymaz *et al.* 2004, 2007a). As commonly emphasized, the NAFZ and surrounding region are important contributors to the seismotectonics of the Anatolian region, because they appear to represent a geological knot where many different tectonic belts converge (Ketin 1966; Görür *et al.* 1998; Okay & Tüysüz 1999; Taymaz *et al.* 2007a, b; Figs 1b and c). The Intra-Pontide and İzmir-Ankara-Erzincan Suture Zones (IAESZ), İstanbul Zone, Sakarya Zone, Central Pontides, Kırşehir Massif, Ezine Pazarı–Sungurlu Fault and the Çankırı Basin are examples of these tectonic structures (Fig. 1b). The 2000-km-long İzmir-Ankara-Erzincan Suture Zone (Fig. 2b), a remnant of the Neo-Tethys Ocean and a major compressional palaeotectonic structure in northern Turkey, trends in an approximately E–W direction to the west of Ankara, then turns nearly 90° and has a NNE trend towards Çankırı (see Koçyiğit 1991; Okay & Tüysüz 1999; Kaymakçı 2000; Taymaz *et al.* 2007a,b). The Çankırı Basin is located between the Sakarya Continent to the north and the Kırşehir Block to the south and bounded by the North Anatolian Ophiolitic Mélange in the west, north and east (Fig. 1c). It has a basement consisting of an upper Cretaceous ophiolitic mélange and granitoids of the Kırşehir Block (Kaymakçı *et al.* 2009, 2010; Robertson *et al.* 2009). Due to its multideformational geological history, the Çankırı Basin and surrounding region have been the focus of several

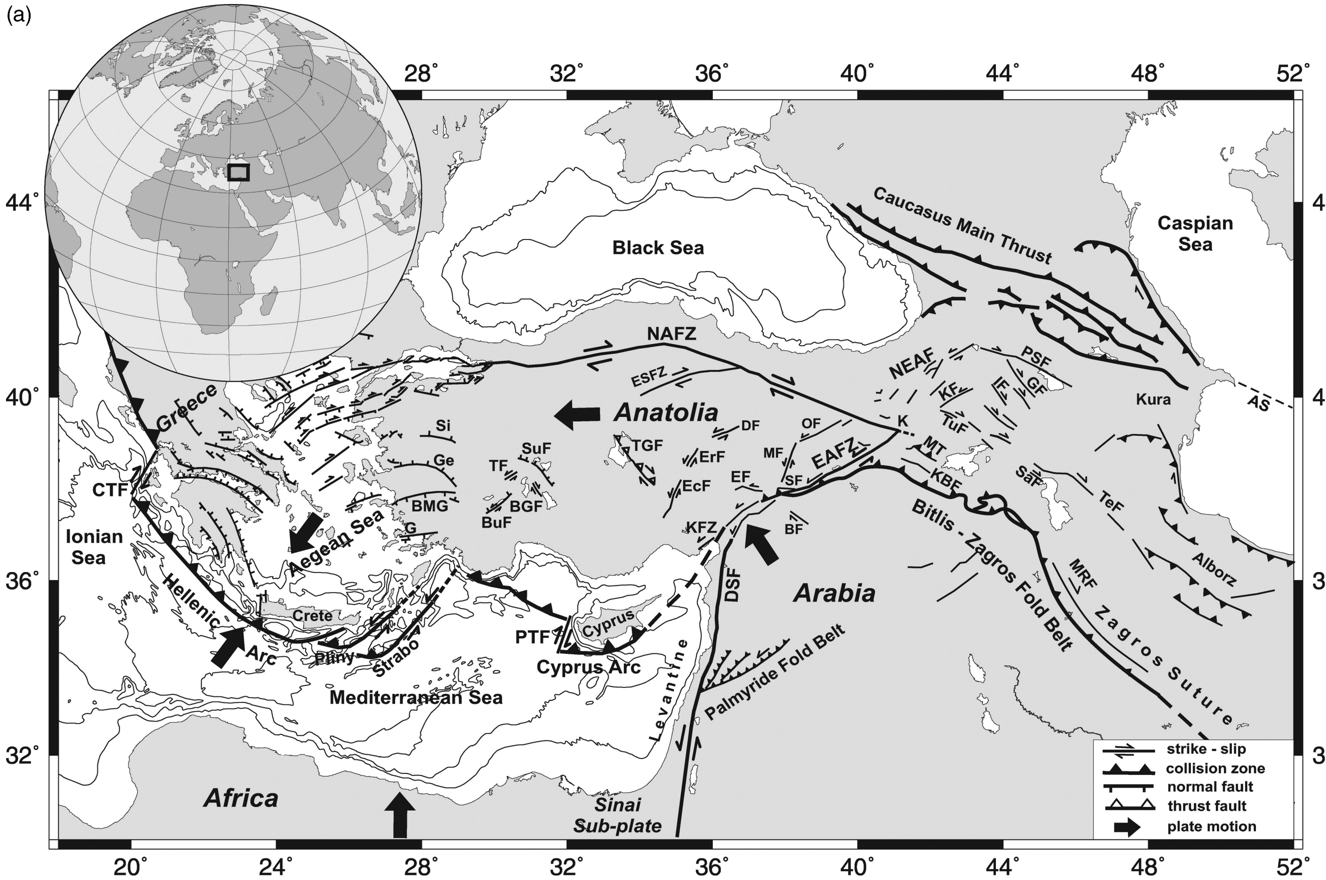

Figure 1. (a) Major tectonic units and bathymetry in the Eastern Mediterranean Sea region (see for details Taymaz *et al.* 2004, 2007a,b; Yolsal *et al.* 2007; Yolsal 2008 and Yolsal & Taymaz 2010). NAFZ, North Anatolian Fault Zone; NEAF, North East Anatolian Fault; EAFZ, East Anatolian Fault Zone; DSF, Dead Sea Transform Fault; AS, Apşeron Sill; BF, Bozova Fault; BGF, Beyşehir Gölü Fault; BMG, Büyük Menderes Graben; BuF, Burdur Fault; CTF, Cephalonia Transform Fault; DF, Deliler Fault; EcF, Ecemiş Fault; EF, Elbistan Fault; ESFZ, Ezine Pazarı–Sungurlu Fault Zone; ErF, Erciyes Fault; G, Gökova; Ge, Gediz Graben; GF, Garni Fault; IF, Iğdır Fault; K, Karlıova; KBF, Kavakbaşı Fault; KF, Kağızman Fault; KFZ, Karataş-Osmaniye Fault Zone; MF, Malatya Fault; MRF, Main Recent Fault; MT, Muş Thrust; OF, Ovacık Fault; PSF, Pampak-Savan Fault; PTF, Paphos Transform Fault; SaF, Salmas Fault; Si, Simav Graben; SuF, Sultandağ Fault; TeF, Tebriz Fault; TF, Tatarlı Fault; TGF, Tuz Gölü Fault; TuF, Tutak Fault. Large black arrows show relative plate motions with respect to Eurasia (McClusky *et al.* 2000, 2003). Bathymetric contours are shown at 500, 1000, 1500 and 2000 m, and are obtained from GEBCO-BODC (1997) and Smith & Sandwell (1997a,b). (b) Major tectonic units and blocks in Turkey. AFZ, Almus Fault Zone; CAFZ, Central Anatolian Fault Zone; DFZ, Dodurga Fault Zone; ETGFZ, Eskişehir-Tuz Gölü Fault Zone; EFZ, Eldivan Fault Zone; LFZ, Laçin Fault Zone; ESFZ, Ezine Pazarı–Sungurlu Fault Zone; KFZ, Kızılırmak Fault Zone; ODFZ, Orta–Devrez Fault Zone; ÇKFZ, Çerkeş–Kurşunlu Fault Zone (revised from Bozkurt & Koçyiğit 1996; Koçyiğit & Beyhan 1998; Okay & Tüysüz 1999; Kaymakçı 2000; Koçyiğit *et al.* 2001; Kaymakçı *et al.* 2003; Taymaz *et al.* 2007b). (c) Generalized geological map of the North Anatolian Fault Zone (NAFZ) in north-central Anatolia showing the Çankırı Basin (Okay & Tüysüz 1999; Taymaz *et al.* 2007b).

geological, seismological and geophysical studies (e.g. Görür *et al.* 1984; Şengör *et al.* 1985; Piper *et al.* 1996; Ateş *et al.* 1999; Kaymakçı 2000; Adıyaman *et al.* 2001; Kaymakçı *et al.* 2003, 2009, 2010; Taymaz *et al.* 2007a,b; Seyitoğlu *et al.* 2009). In northern-central Anatolia, this study area, there are also several small- and large-scale sedimentary basins (e.g. Çerkeş-Kurşunlu-Ilgaz, Tosya, Kargı, Vezirköprü, Havza–Ladik, Niksar, Suşehri, Erzincan and Karlıova) associated with bends and offsets of the strike-slip fault zones.

The North Anatolian Fault (NAF) is analogous to the San Andreas Fault (SAF) in California in some ways, with the two continental transforms sharing similar slip rates, total fault length and straightness relative to their poles of rotation (Stein *et al.* 1997). However, the age and offset values are significantly different for each fault zone. The NAF is younger (∼5 Ma) than the SAF (∼17–30 Ma) and has about 85 km of cumulative displacement (Westaway 1994; Armijo *et al.* 1999; Barka *et al.* 2000; Hubert-Ferrari *et al.* 2009) compared to the SAF, which has ∼315–730 km of offset (e.g. McKenzie & Morgan 1969; Atwater 1970; Dickinson & Wernicke 1997). Similar in large earthquake activity with the SAF, the NAF constitutes the northern boundary of the Anatolian Plate. The scattered earthquake activity along the NAF and the abundance of off-fault seismicity might be an indication of its young age and geological and structural complexity. Fig. 2(a) shows recent seismicity in the Eastern Mediterranean and surrounding region reported by the USGS-NEIC (United States Geological Survey – National Earthquake Information Center; 1973–2010) and focal mechanism solutions of major earthquakes ($M > 6.0$) along the NAFZ. Major destructive earthquakes occur on the NAFZ with a westward migrating pattern, from the Karlıova Triple Junction to the Marmara region, in series, every ∼200–400 yr, causing serious risk for population centres (for details see Barka 1996; Stein *et al.* 1997; Ambraseys 2002). One of the largest historical earthquakes occurred in 1939, in Erzincan, eastern Turkey

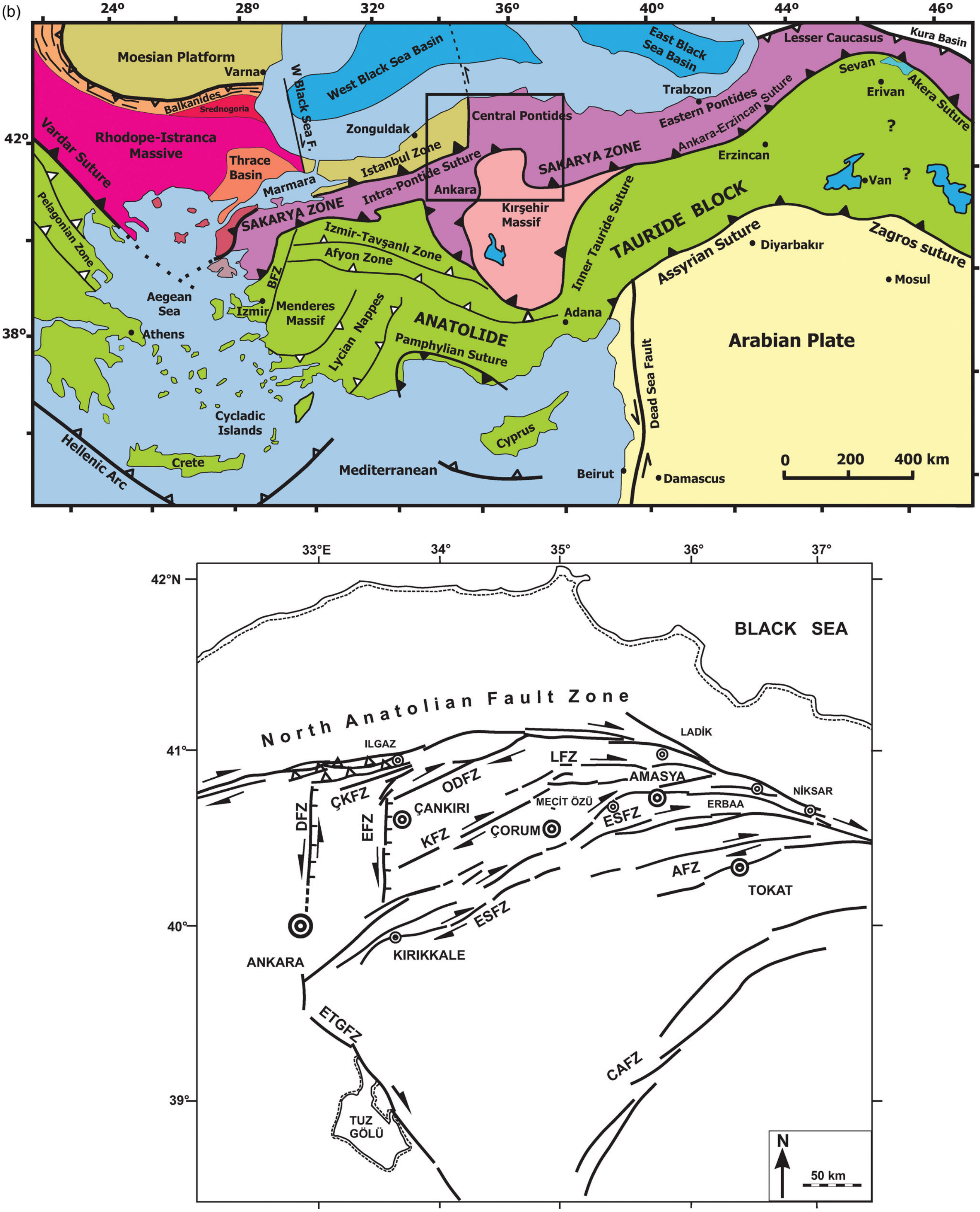

Figure 1. (*Continued.*)

(M_w 7.9) and ruptured over 360 km of the NAFZ, with a maximum right-lateral offset of ∼7.5 m. The seismicity (Fig. 2a) progressed along the fault zone with many $M_s > 6$ earthquakes, reaching Hersek Peninsula and beyond with the recent 1999, M_w 7.6 and 7.2 İzmit and Düzce earthquakes, respectively (Barka *et al.* 2000).

In this study we used local earthquake tomography (LET) to obtain a better understanding of the 3-D *P*-wave crustal structure

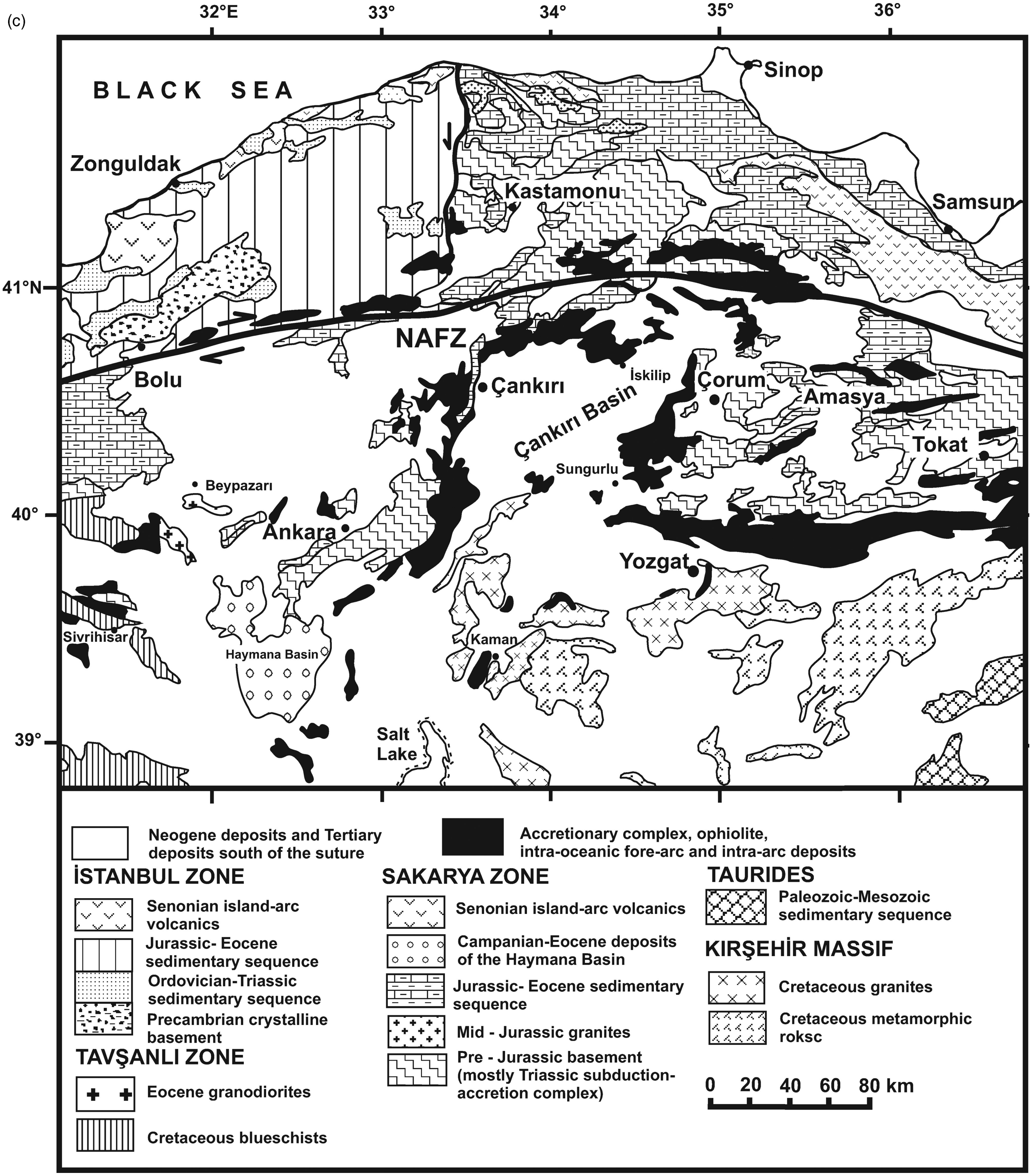

Figure 1. (*Continued.*)

and V_p/V_s ratios for the region. LET studies are able to image heterogeneities in the crust and upper mantle, with spatial resolution depending on the density of ray sampling (e.g. Thurber 1981, 1992). Many local tomography studies have been performed during the last decade in different tectonically active regions, including strike-slip, subduction, collisional and/or volcanic zones (see Thurber *et al.* 1997, 2009; Husen *et al.* 2000; Paul *et al.* 2001; Rowlands *et al.* 2005; Koulakov *et al.*, 2007; Kaypak 2008; Haberland *et al.* 2009). A detailed knowledge of the velocity structure of the crust and upper mantle not only helps to improve our understanding of the tectonics of a region, but also plays a key role in obtaining accurate earthquake locations.

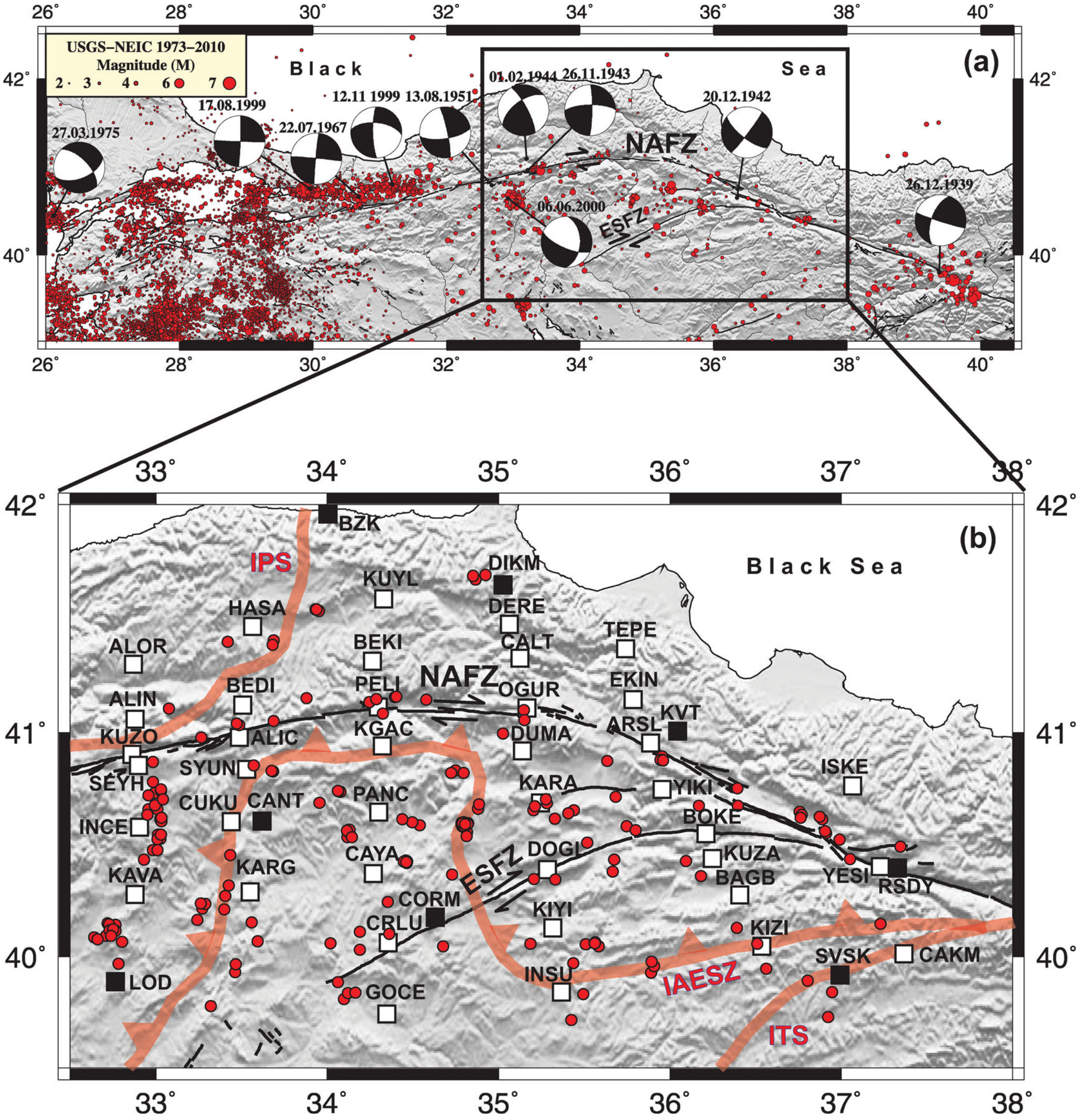

Figure 2. (a) Earthquake activity reported by USGS-NEIC and focal mechanism solutions of major earthquakes ($M > 6.0$) along the North Anatolian Fault Zone (NAFZ) and surrounding region for the period of 1973–2010 (Table B1; compiled from McKenzie 1972; Taymaz *et al.* 1991, 2007b; Taymaz 1999; Şengör *et al.* 2005) and (b) the setting of the NAF Passive Seismic Experiment in the north-central Anatolia. The seismic network (white squares) consisted of NAF broad-band stations operating from 2006 January to 2008 May. The black squares denote KOERI (Kandilli Observatory) stations used to improve the azimuthal coverage in this study (see Table 1). New earthquake ($M \geq 3.0$) locations obtained by using the ANTELOPE dbloc2 commercial software suite from BRTT (1998) and P and S readings recorded by NAF and KOERI stations are also shown. Black lines indicate the major faults (Şaroğlu *et al.* 1992) and red the suture zones (Okay & Tüysüz 1999) in the region, respectively. IAESZ, İzmir-Ankara-Erzincan Suture Zone; ESFZ, Ezine Pazarı–Sungurlu Fault; NAFZ, North Anatolian Fault Zone; ITS, Intra-Tauride Suture; IPS, Intra-Pontide Suture.

Despite numerous geological and geophysical studies, the shallow complex structures in north-central Anatolia remain poorly understood. After the devastating 1999 İzmit and Düzce earthquakes, the Marmara Sea Basin and the western part of the NAFZ were investigated in numerous seismological studies. Several tomography studies were performed to understand the shallow crustal structure of the western continuation of the NAFZ (e.g. Nakamura *et al.* 2002; Karabulut *et al.* 2003; Barış *et al.* 2005; Salah *et al.* 2007; Becel *et al.* 2010; Koulakov *et al.* 2010). In contrast, there is still no detailed information about the 3-D crustal velocity structure and deformation styles in the central part of the NAFZ, even though it has been extensively studied by various methods (e.g. Tatar *et al.* 1996; Gürbüz *et al.* 2003; Toksöz *et al.* 2003; Kuleli *et al.* 2004; Şengör *et al.* 2005; Taymaz *et al.* 2007a,b; Tok *et al.* 2008; Gans *et al.* 2009; Biryol *et al.* 2010). To image the crustal structure in north-central Anatolia, Gürbüz *et al.* (2003) carried out seismic refraction studies, which suggested the crust is about 36 km thick at south of NAFZ, and decreases to 30 km north of the NAFZ, with an average P_n velocity of 7.8 km s^{-1}. Similarly, Kuleli *et al.* (2004) found that the crustal thickness varies between 37 and 42 km in central Anatolia, with a P_n velocity of about 8 km s^{-1}, also based on seismic refraction data. They observed laterally changing crustal thickness and an abrupt change across the major fault zones, such as the NAFZ, suggesting that the crustal thickness is thinner in northwest Anatolia and slightly thicker in eastern Anatolia. Gans *et al.* (2009) performed P_n tomography and reported the lack of a P_n velocity contrast across the NAFZ. They also found that P_n velocities in the Eastern and Western Pontides are slower than in the Central Pontides. In addition, there are a number of crustal models from receiver function studies by Saunders *et al.* (1998), Tok *et al.* (2008) and Çakır & Erduran (2011) for the Anatolian region to name a few among others.

We investigate the shallow crustal structure and seismicity in the central part of the North Anatolian Fault using LET. We used high-quality earthquake data recorded by 47 broad-band seismometers to determine a 3-D *P*-wave velocity model and the V_p/V_s distribution. We compare our tomographic images with well-known geological structures such as the Ezine Pazarı–Sungurlu Fault Zone, Çankırı Basin and İzmir-Ankara-Erzincan Suture Zone.

2 DATA AND METHOD

We used 39 broad-band seismic stations installed in the study area starting in 2006 January and operating until 2008 May, as a part of the 'North Anatolian Fault (NAF) passive seismic experiment', a joint project between the University of Arizona, Istanbul Technical University, Middle East Technical University and Boğaziçi University Kandilli Observatory and Earthquake Research Institute (KOERI; http://www.koeri.boun.edu.tr/, last accessed 2010). We also complemented our stations with additional data from eight permanent broad-band KOERI network stations located in the same region (Table 1, Fig. 2b).

The data set includes arrival times of *P*-waves and *S–P* times obtained from ∼300 local earthquakes ($M \geq 3.0$) that occurred within north-central Anatolia for the period of 2006 January–2008 May. Arrival times of 9890 *P* and 7917 *S* waves were picked on vertical and horizontal components using the ANTELOPE commercial software suite from Boulder Real-Time Technologies (BRTT 1998). The Wadati diagram and traveltime versus distance graphs were plotted to estimate the average V_p/V_s ratio (1.76), as well as the direct and refracted crustal *P*- and *S*-wave velocities (Figs 3 and 4). We were able to locate about 200 earthquakes, which had at least six *P* and *S* readings, with an azimuthal gap of less than 200°, using ANTELOPE dbloc2 algorithm package and the velocity model of Gürbüz *et al.* (2003) and Toksöz *et al.* (2003). In the final inversions, only 168 earthquakes were selected based on their azimuthal gap in station coverage (≤180°), the number of *P*- and *S*-wave readings (>at least 10 *P*-wave arrivals) and small rms values (Fig. 2b).

Table 1. Coordinates of broad-band seismic stations which belong to the 'NAF Passive Seismic Experiment' and KOERI used in this study (see Fig. 2b).

Station	Lat. (°N)	Lon. (°E)	Station	Lat. (°N)	Lon. (°E)
ALIC	40.978	33.487	INSU	39.842	35.366
ALIN	41.061	32.879	ISKE	40.764	37.067
ALOR	41.301	32.870	KARA	40.688	35.245
ARSL	40.955	35.887	KARG	40.291	33.552
BAGB	40.278	36.410	KAVA	40.280	32.878
BEDI	41.121	33.506	KGAC	40.941	34.323
BEKI	41.315	34.263	KIYI	40.131	35.316
BOKE	40.552	36.211	KIZI	40.048	36.536
BZK	41.960	34.003	KUYL	41.590	34.332
CAKM	40.015	37.367	KUZA	40.441	36.248
CALT	41.328	35.125	KUZO	40.904	32.861
CANT	40.606	33.619	KVT	41.008	36.046
CAYA	40.373	34.269	LOD	39.889	32.764
CORM	40.178	34.630	OGUR	41.109	35.165
CRLU	40.064	34.357	PANC	40.647	34.301
CUKU	40.604	33.441	PELI	41.113	34.299
DERE	41.477	35.064	RSDY	40.397	37.327
DIKM	41.649	35.025	SEYH	40.856	32.900
DOGL	40.391	35.284	SVSK	39.917	36.992
DUMA	40.918	35.140	SYUN	40.838	33.529
EKIN	41.147	35.787	TEPE	41.369	35.743
GOCE	39.743	34.348	YESI	40.405	37.229
HASA	41.469	33.565	YIKI	40.748	35.954
INCE	40.581	32.906			

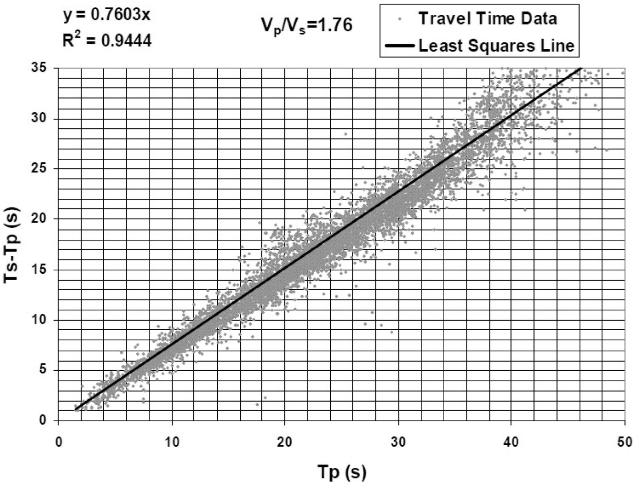

Figure 3. Wadati diagram using *P*- and *S*-wave traveltimes recorded by the NAF Experiment and KOERI stations used in this study. Tp, *P*-wave traveltime; Ts, *S*-wave traveltime. The approximate V_p/V_s ratio is 1.76 for the north-central Anatolia region.

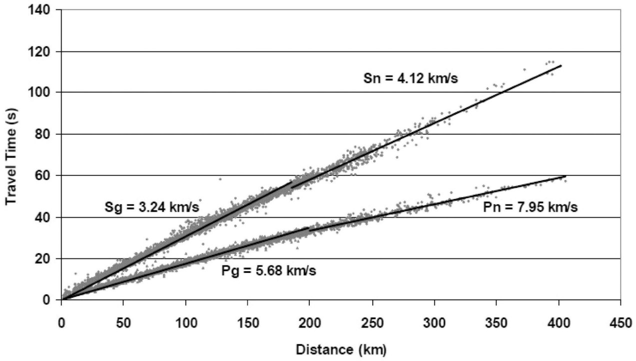

Figure 4. Traveltime V_s. distance plot indicating average direct and refracted crustal *P*- and *S*-wave velocities.

2.1 1-D velocity inversion

To obtain an appropriate 1-D starting model, we computed the best minimum 1-D *P*-wave velocity model using the VELEST code (Kissling 1988; Kissling *et al.* 1994, 1995). This algorithm calculates the ray paths from source to receiver, including direct, refracted and reflected rays passing through the given 1-D velocity model. Because the problem is non-linear, the solution is obtained iteratively. The inversion process consists of checking the space parameters, taking into account different 1-D initial models that include varying the numbers of initial velocities and thicknesses of the layers. It

Table 2. The final 1-D *P*-wave velocity model obtained for the study area.

Layer depth (km)	Layer thickness (km)	V_p (km s^{-1})
–2.0	–2.0	2.15
0.0	5.0	3.86
5.0	2.0	5.66
7.0	2.0	5.99
9.0	2.0	6.09
11.0	4.0	6.10
15.0	5.0	6.18
20.0	10.0	6.20
30.0	10.0	6.62
40.0*	10.0	7.67
50.0*	–	8.10

∗Denotes an undetermined layer velocity by the 1-D inversion.

also calculates station corrections to compensate for heterogeneous velocity structure near individual stations (Douglas 1967; Pujol 1988; Searcy 2003). Further details of the processing steps for the VELEST code can be found in Kissling (1988) and Kissling *et al.* (1994, 1995).

We applied the VELEST code in a simultaneous mode, inverting for both velocity and hypocentre locations. We chose layering of the starting 1-D velocity model in accordance with refraction seismic studies carried out in this region (Gürbüz *et al.* 2003; Toksöz *et al.* 2003). Because the VELEST code does not alter layer geometry and involves a trial-and-error process, we performed trial runs for several models with different layering and velocities to select the best-fitting layer thickness and geometry, and thus to establish the best minimum 1-D model. The velocity model giving the minimum rms value (0.51) was chosen as the final 1-D *P*-wave velocity model (Fig. 5 and Table 2). The layers at 40 and 50 km depth are poorly constrained due to the absence of deep earthquakes in the study area. The inversion results were tested by using many initial models with average velocities significantly higher and lower than those of the starting 1-D model. However, we calculated high rms values for both trial cases. We used damping parameters of 0.01 for the hypocentral, 0.1 for the station and 1.0 for the velocity parameters, as suggested by Kissling (1988) and Kissling *et al.* (1994).

To calculate *P*-wave station corrections, we selected station PELI as the reference station because of its central location within the network and the abundance of recorded earthquakes (Fig. 2b). Station corrections represent the averaged characteristics of local surface geology at each site (Kissling 1988; Husen *et al.* 2000, 2003). In our case, small station delays were obtained in the central part of the seismic network, whereas large *P*-wave station corrections (>0.7 s) were found towards the outer regions of our study area (Fig. 6). Negative station delays correspond to having true velocities faster than the model, and positive delays to true velocities slower than the model. Absolute station delay values tend to be larger at the outside of the network due to the combined effects of local geology and the limited azimuthal coverage and distances of observations at these stations. Thus the resultant 1-D velocity model is a better representation of the structure in the well-sampled central parts and deviates more from the structure in the peripheral regions and structure beneath corresponding stations. This deviation might be mapping into station corrections (and compensated by these terms) of the peripheral stations, making them larger.

Next, we determined new earthquake hypocentres using the best minimum 1-D *P*-wave velocity model, *P*-wave station corrections and traveltimes of local *P* and *S* waves in the single event mode of the VELEST algorithm. We also plotted approximate ray coverage using lines to connect individual stations and events (Fig. 7). These rays demonstrate the capability of resolving power for each grid node in the 3-D LET inversion.

2.2 3-D LET

We used the damped least-squares iterative inverse code SIMULPS14, which includes a standard approximate pseudo-bending ray tracer (ART) and a full 3-D shooting ray tracer algorithm (RKP, Eberhart-Phillips 1990, 1993; Virieux & Farra 1991; Evans *et al.* 1994; Husen *et al.* 2000; Haslinger & Kissling 2001), to invert for the 3-D velocity models. The final data set consists of 168 well-located earthquakes recorded by 47 broad-band seismic stations, with 5444 *P*-wave and 3200 *S*-wave arrival times. The velocity model is specified on a set of 3-D spatial gridpoints, with a linear interpolation adopted between the points, consistent with the previous LET studies cited earlier. We constructed the initial *P*-wave velocity model using the best minimum 1-D horizontally layered model determined from the VELEST code, and a reference V_p/V_s value of 1.75. We initially tried several different grid intervals, varying between 15 and 30 km, to obtain the optimum grid settings for the inversion. A final grid spacing of 25 km × 25 km in the horizontal directions was chosen for the central part of the study area, due to the dense ray path coverage and station distribution (Fig. 7). Grid nodes in the vertical direction were positioned at –2, 0, 5, 7, 9, 11, 15, 20, 30, 40 and 50 km, consistent with our best 1-D *P*-wave velocity model (Table 2). The thin vertical node layering between 5 and 11 km yielded low rms values for the initial 1-D starting model and initial earthquake locations. The thin layers allow better modelling of vertical gradients which improves ray tracing for rays bottoming in this depth range and provide model flexibility to more accurately reflect topography of the basin–basement interface. Model resolution studies shown later indicate that there is some decline in individual parameter resolution but we did not interpret individual node anomalies in the resulting tomography. Another important input parameter is the minimum number of rays sampling in each grid node; the resolution of the inversion improves as the number of rays increases. Using a trial-and-error method, we chose a minimum of five rays for both the synthetic and the real models. Based on previous studies, the crustal thickness was assumed to be about 40 km for the entire model and to account for arrivals of P_{n} phases, the upper-mantle part of the model was constrained by a deeper layer located at 50 km. Throughout the tomography inversion, we applied weighting to each observation based on both residual size and source–receiver distance. We also tested variability with larger and equal layer grid node spacing and obtained very similar results for the well-resolved central portion of our modelled region (see Appendices A and B).

One of the key parameters in the inversion is the damping value, which depends on the earthquake source-station distribution and the selected grid intervals. The damping parameter influences both the inversion results and resolution estimates (e.g. Husen *et al.* 2000; Kissling *et al.* 2001). In this study, we followed the Eberhart-Phillips (1986) procedure to select the appropriate damping value by evaluating trade-off curves between the data and the solution (model) variances. These trade-off curves are built with a single iteration

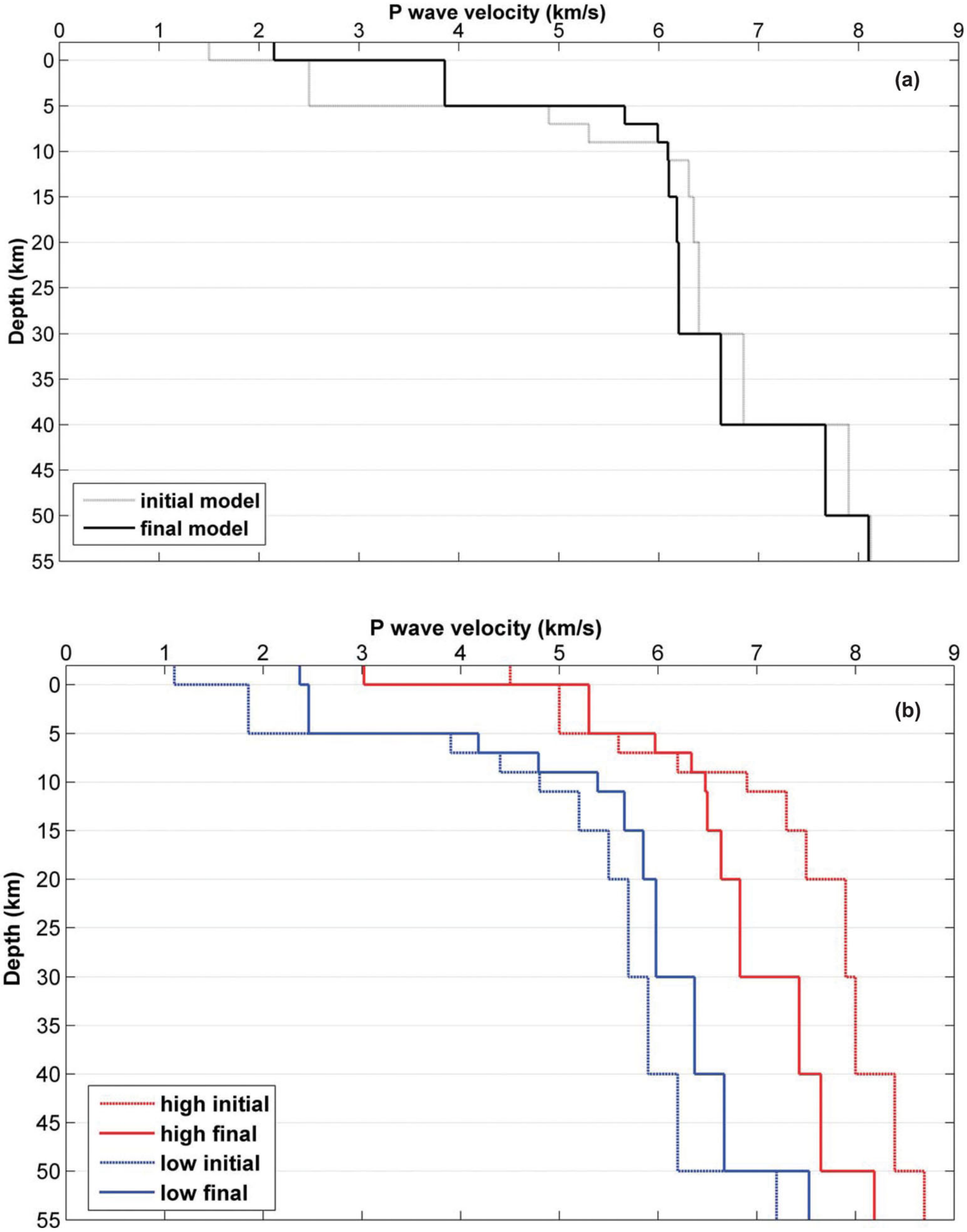

Figure 5 (a) The final 1-D P-wave velocity model (black solid line) after several inversion steps (for model details see Table 2). The dashed line shows the starting (initial) 1-D velocity model used in the inversion. (b) Tests on the stability of the minimum 1-D P-wave velocity model. The dashed lines indicate the input models for the tests with high and with low initial velocities, and the solid lines represent the resulting models after the inversion.

inversion for the coupled hypocentre-model parameters, using a wide range of damping parameters. Because suitable damping values show a significant decrease in data variance without a strong increase in model variance, we chose a damping value of 50 for both V_p and V_p/V_s inversions based on the calculated trade-off curves and Occam's Razor approach (Fig. 8). A damping parameter of 10 also produces the same data variance, but its calculated model variance is higher. According to the Occam's Razor approach, if two models give the same misfit, the tendency is to choose the simplest model (e.g. smallest number of parameter, smallest size and smoothest; see Trampert & Spetzler 2006).

Additional criterion describe the resolution of the tomography results, including the number of ray hits contributing to one particular node (KHIT), the derivative weighted sum (DWS, geometric average) and the diagonal element of the resolution matrix, resolution diagonal element (RDE, see Haslinger *et al.* 1999; Husen *et al.* 2000; Dias *et al.* 2007; Kaypak 2008; Arroyo *et al.* 2009; Thurber *et al.* 2009). For example, the DWS value defines the relative ray density in the vicinity of a model parameter (Thurber & Eberhart-Phillips 1999) and is a better measure of information density provided by the ray coverage than counting the number of rays. The RDE is the best and quickest estimation of the quality of the solution, however, as it presents the degree of independence of the model parameters in the solution. All resolution parameters are affected by the chosen model parametrization of the tomography inversion (Husen *et al.* 2000, 2004; Kissling *et al.* 2001).

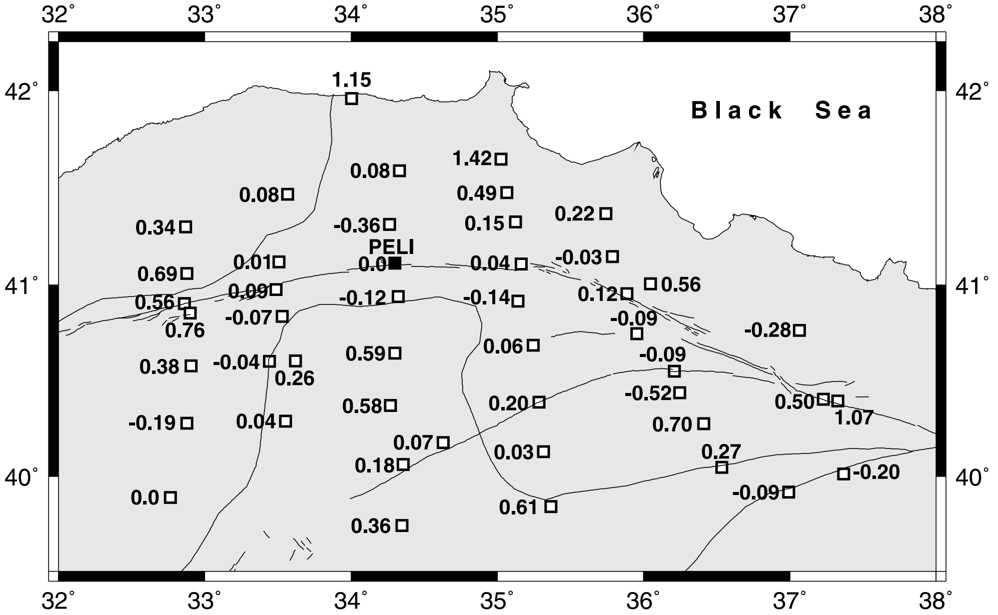

Figure 6. *P*-wave station corrections obtained from the best 1-D *P*-wave velocity model inversion (relative to station PELI).

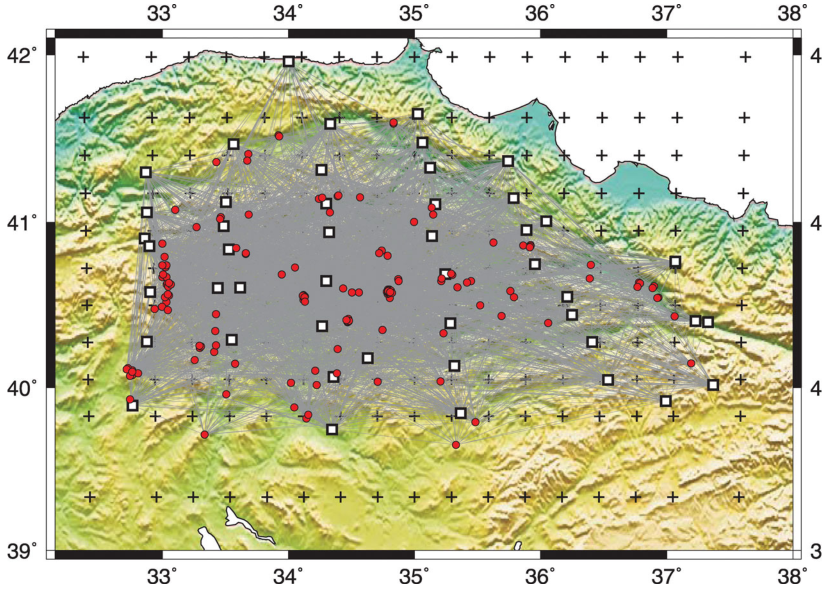

Figure 7. Hypocentre locations of 168 selected earthquakes obtained from the VELEST single event location and ray path coverage (thin grey lines) for 3-D *P*-wave local earthquake tomography. Plus signs and white squares represent 25 km × 25 km horizontal grid node spacing (for interior parts) and seismic broad-band stations, respectively.

3 RESOLUTION AND RESULTS

The 3-D *P*-wave velocity and V_p/V_s ratio models were obtained by performing two separate but sequential inversion steps, each having six iterations, using the inversion control parameters described earlier. The output of the first inversion was introduced as the input to the second inversion. After the final inversion, we reduced the rms traveltime residual from 0.51 s (rms for 1-D *P*-wave velocity inversion) to 0.077 s (rms after 3-D *P*-wave inversion) and 0.078 s (rms after 3-D V_p/V_s inversion).

3.1 Resolution

As commonly emphasized, complex 3-D velocity structures derived from LET can only be interpreted meaningfully if the model's quality is known (e.g. Thurber 1993; Husen *et al.* 2000; Arroyo *et al.* 2009). We therefore plotted the resolution control parameters such as DWS and RDE (Fig. 9). Further, we used checkerboard sensitivity tests, which are useful in assessing the ability of the tomographic inversion to resolve structural details in the Earth, to give a general picture of the resolving power of the inversion. For this purpose,

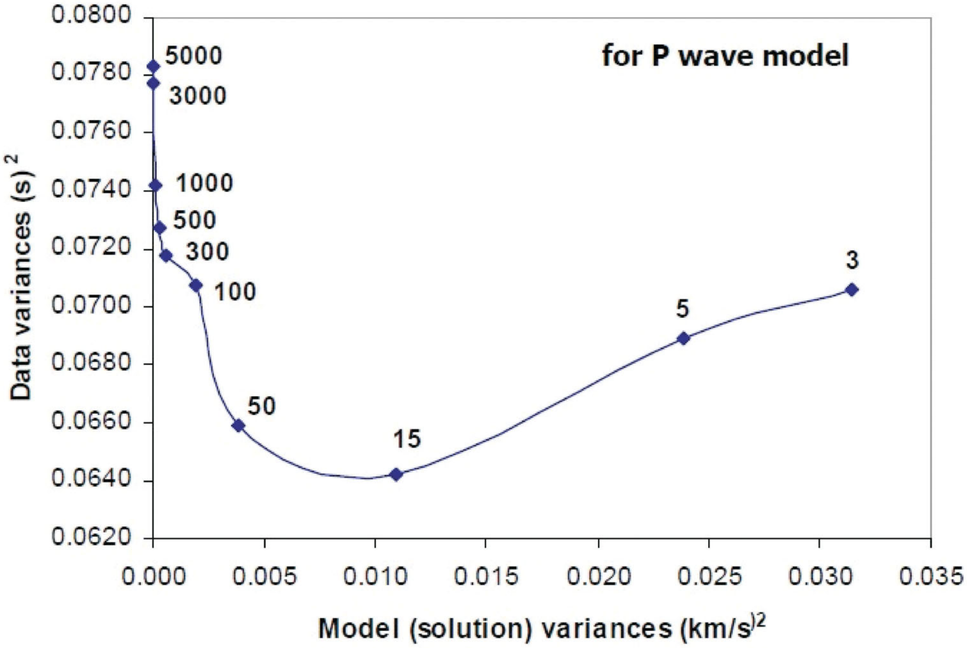

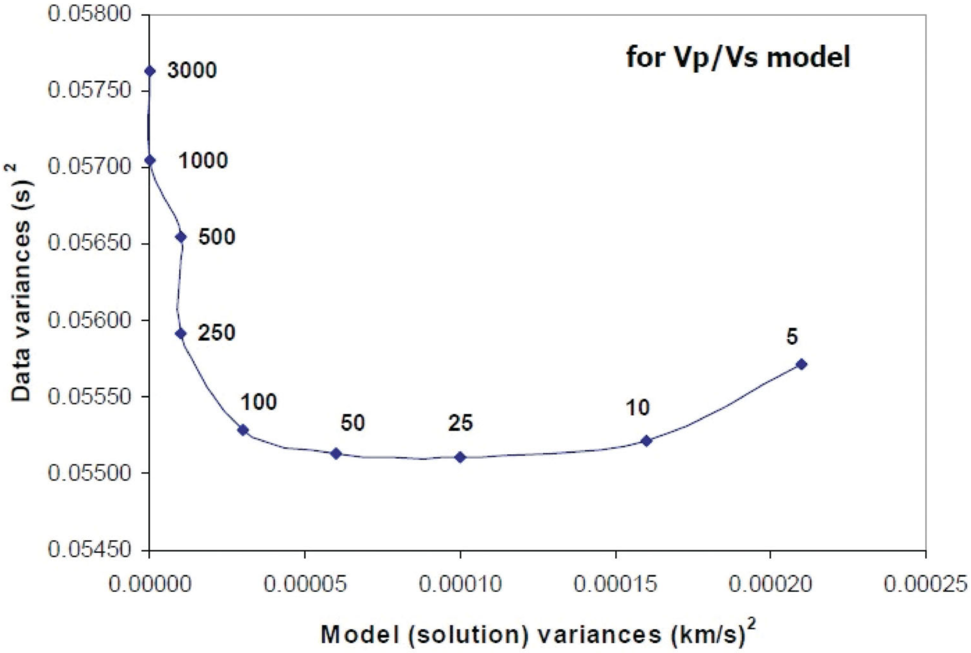

Figure 8. Trade-off curves plotted for different damping values for *P*-wave and V_p/V_s ratio one-iteration inversions. We chose a damping value of 50 for both inversions.

we set up a checkerboard velocity model by adding ±5 per cent velocity variation to our initial model, and generating synthetic *P*-wave traveltimes from each earthquake hypocentre to the recording stations. The velocity perturbations are a percentage of the actual velocity value. Before the inversion, we added Gaussian distributed noise with a standard deviation of 0.1 s, with zero mean, to the synthetic traveltimes. Finally, the synthetic data were inverted using the same parametrization, constraints and control parameters used in the real data inversion (Fig. 10).

We also applied jackknife tests to observe the influence of various groups of earthquakes on the inversion results. For each case, we removed 10 different earthquakes selected randomly from the input data, and then applied the 3-D inversion using the same model parametrization. The mean velocities and standard deviations of velocities were calculated for each gridpoint in each model layer, using the jackknife test results (see Appendix A, Figs A1–A4). The jackknife test and resolution parameters indicate that we have good resolution in the central part of our study area.

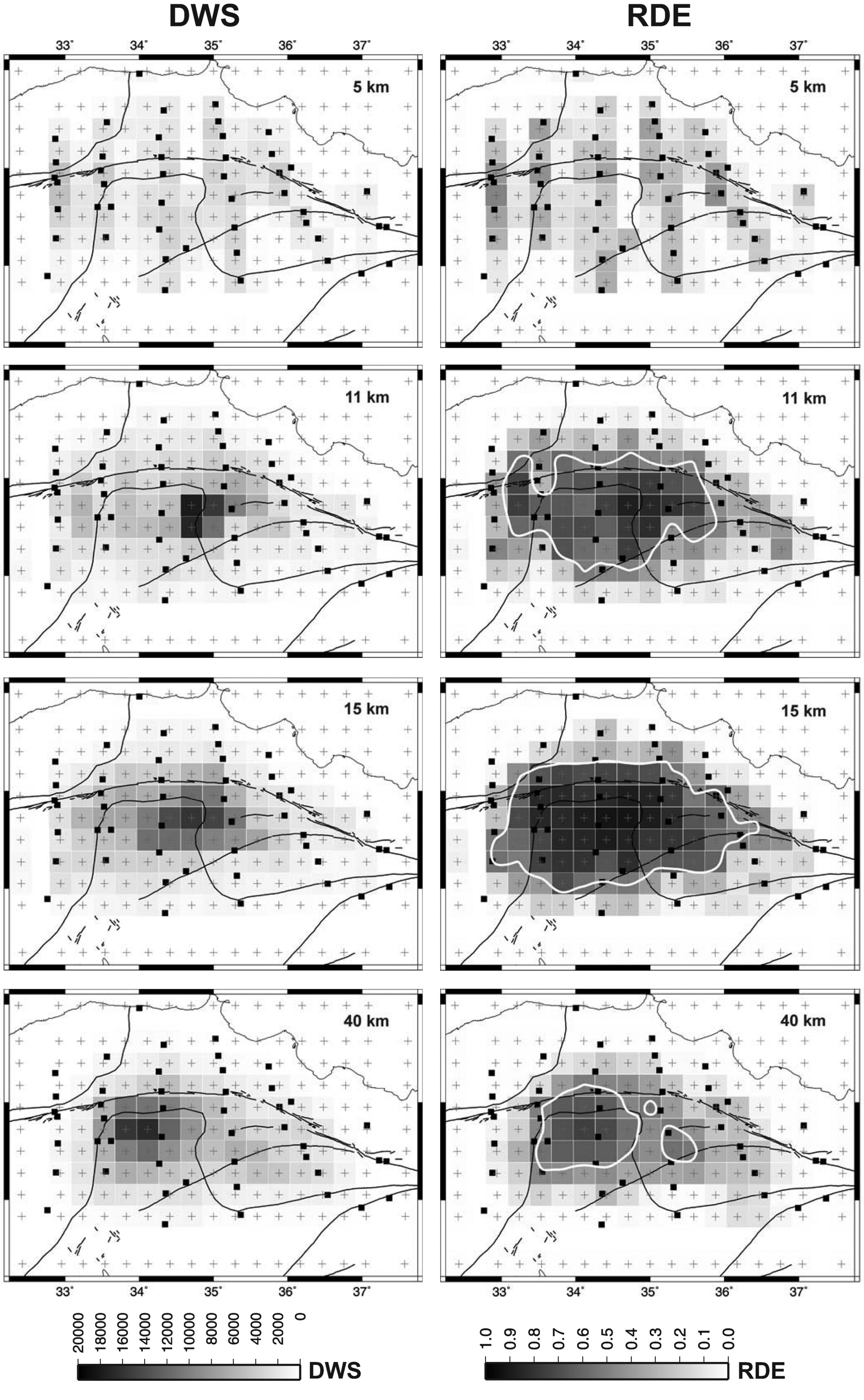

Figure 9. Selected horizontal depth sections of DWS (derivative weighted sum) and RDE (resolution diagonal element) values shown for the final 3-D V_p velocity inversion. Both parameters are used to determine the well-resolved parts of the model. White contours represent the region with good resolution, with an RDE > 0.5. Black lines delineate fault and suture zones in the study area.

Most of the rays are subvertical for the uppermost layers (0–5 km), which means that good resolution is only obtained directly below the seismic stations at these shallow depths. The DWS, RDE values for each node, and thus the resolution at deeper layers (5–30 km) increases in the central part of the study area (Fig. 9). The ray path density is low near the edges of the study area, resulting in poor resolution (Fig. 9); hence, we cannot interpret results at the edges of the region. Test results show similar patterns with the synthetic input data for most parts of the study area, but the amplitude of the velocity perturbation after the inversion slightly decreased for each

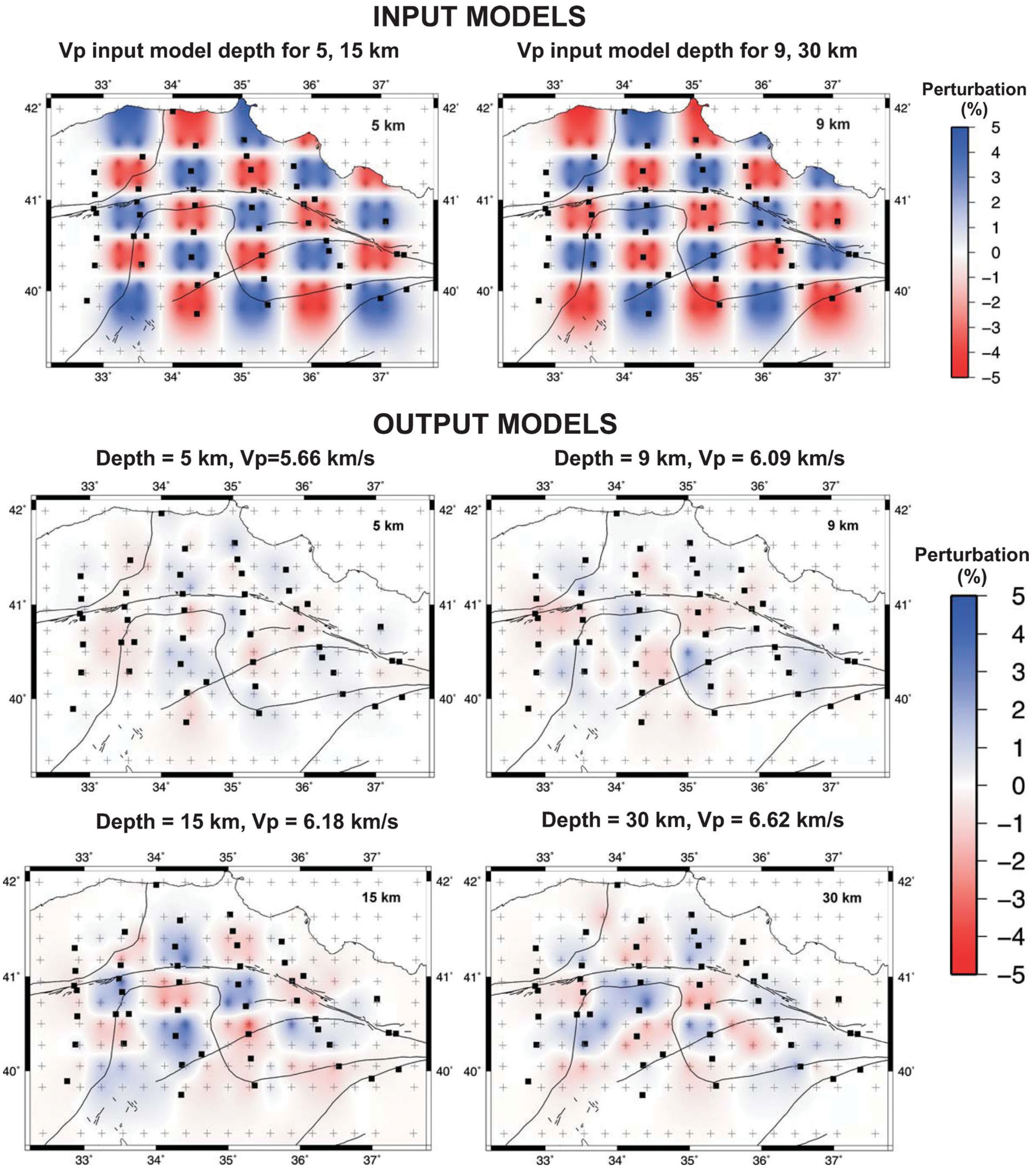

Figure 10. Input and recovered models in V_p checkerboard resolution test. Black squares and grey plus signs show stations and grid intervals, respectively. Faults and sutures are also shown. Depth values and background *P*-wave velocities for each layer are indicated above the map.

layer. For example, at 15 km depth we recovered maximum of 60 per cent of the amplitude of the input model in our output model of the synthetic test. In general, the test results and resolution parameters indicate that our resolution is poor for the uppermost layer (0–5 km, not shown), but is much better in the central part of the region for deeper layers.

The jackknife test results did not show major differences in the amplitudes and locations of the major velocity anomalies when various groups of earthquakes were randomly removed for each test (see Appendix A, Figs A4 and A5). There are some moderate changes in the amplitudes of anomaly A, C1 and C2 in the jackknife test, but in most cases we can still identify all the major anomalies. Overall, resulting tomographic models show small variations for individual tests, suggesting that these structures are robustly resolved and their outlines and associated V_p values are not affected by random variations in the data set (see Appendix A, Figs A4 and A5).

3.2 3-D *P*-wave velocity inversion

Final hypocentre locations and focal depths of 168 earthquakes are plotted in both map view and vertical E–W and N–S cross-sections in Fig. 11. We observe that the distribution of

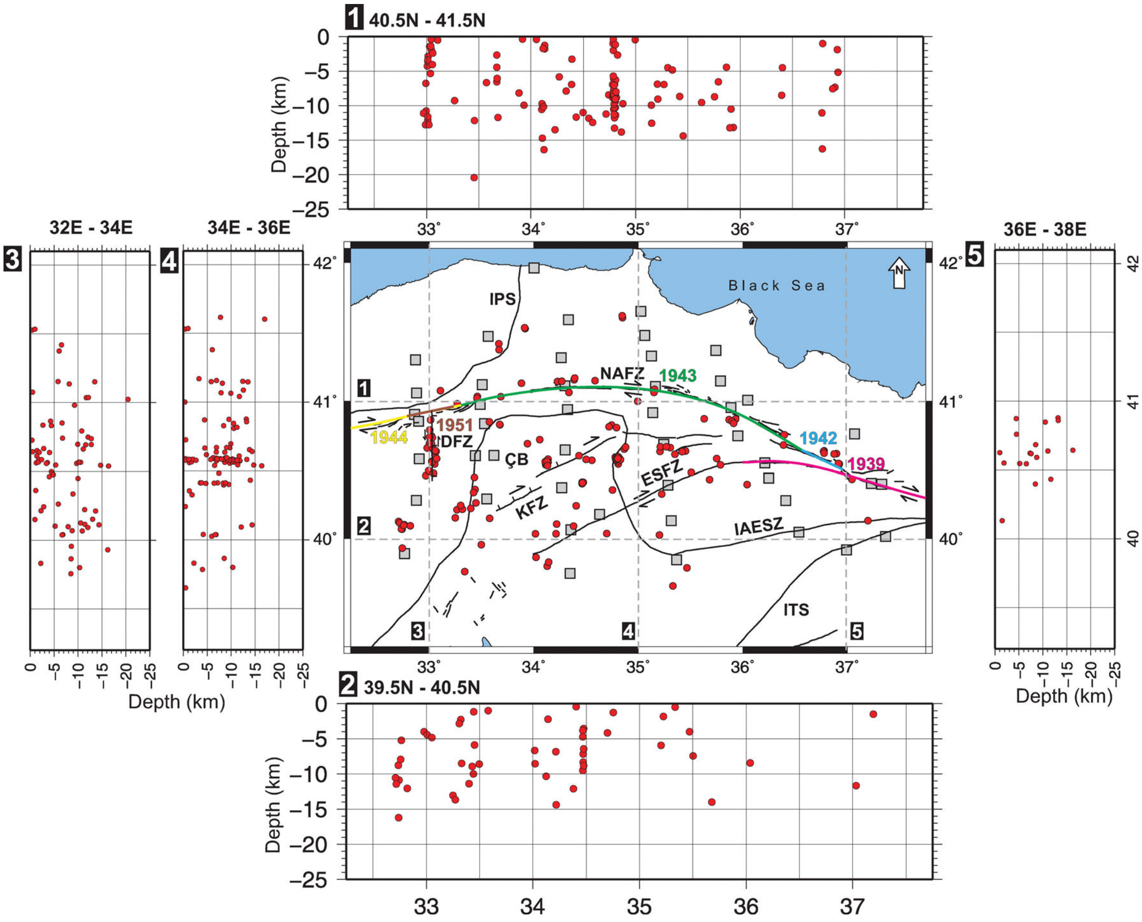

Figure 11. Final hypocentre locations of 168 earthquakes obtained from 3-D *P* wave velocity inversion, shown in map view and vertical cross-sections in E–W and N–S directions. The pattern and character of ruptured segments of the NAFZ by the events that occurred in the past century are illustrated with coloured lines (McKenzie 1972; Barka 1996; Stein *et al.* 1997). Grey squares are broad-band stations used in inversion. NAFZ, North Anatolian Fault Zone; ESFZ, Ezine Pazarı-Sungurlu Fault Zone; KFZ, Kızılırmak Fault Zone; ÇB, Çankırı Basin; DFZ, Dodurga Fault Zone; IAESZ, Izmir-Ankara-Erzincan Suture; IPS, Intra-Pontide Suture; ITS, Intra-Tauride Suture. Cross-sections cover 1° and 2° compressed total area for E–W and N–S profiles, respectively. Faults and sutures are taken from Okay & Tüysüz (1999), Koçyiğit *et al.* (2001), Taymaz *et al.* (2007a,b) and Kaymakçı *et al.* (2009, 2010).

seismicity appears mostly concentrated at shallow crustal depths ($\leq$15 km). After the inversion, relocated earthquakes are spatially correlated with surface traces of multiple strike-slip faults corresponding to segments of the NAFZ and its splays (Fig. 11).

The *P*-wave velocity perturbations for individual model layers indicate comparatively abrupt and high velocity changes relative to the 1-D *P*-wave model for parts of north-central Anatolia (Fig. 12). In particular, these higher velocity regions have *P*-wave velocities greater than 6.5 km s^{-1} below 15 km depth. The relatively lower *P*-wave velocities ($6.0 \leq V_p \leq 6.5$ km s^{-1}) within the tomographic model have limited lateral extents and vertically descend down to the depths of 20 km (Fig. 13). These features can be clearly seen in profile 3 in Fig. 13(a). In addition, very low *P*-wave anomalies on the order of –2 to –3 per cent are observed at the centre of the study area, and along segments of the NAFZ (see Fig. 12).

3.3 3-D V_p/V_s inversion

The V_p/V_s inversion requires the use of *S*-wave arrival times in addition to *P*-wave data. In general, *S*-wave velocity model solutions tend to have lower resolution and greater uncertainty than *P*-wave models, as there tend to be fewer *S*-wave observations. In addition, *S* waves are more difficult to pick and anisotropy can also be a problem. *S* waves can help the LET problem, however, by increasing constraints on earthquake source depths and providing information that helps to decouple the hypocentres from the structure (Thurber 1993). The aim of inverting for V_p/V_s instead of V_s is based on the assumption that V_p/V_s is a better estimate from an initial average V_p/V_s value than from a homogeneous V_s model in areas of lower V_s and higher V_p resolution (Eberhart-Phillips & Reyner 1997). Initially, the V_p/V_s value in the inversion was set to 1.76 for north-central Anatolia, based on the Wadati diagram shown in this study (Fig. 3). After several 3-D inversion steps, notable variation in V_p/V_s values between 1.70 and 1.82 were observed throughout the study region. In most of the profiles, high V_p/V_s values ($\geq$1.80) were located within north-central Anatolia (Figs 14a and b). The distribution of high and low V_p/V_s values within the model, while rather complex and heterogonous, tends to have vertical orientations for most of the volumes associated with high V_p/V_s values (Fig. 14).

4 DISCUSSION

In this section the *P* wave and V_p/V_s tomography results are discussed, as well as the final earthquake locations. Most of the

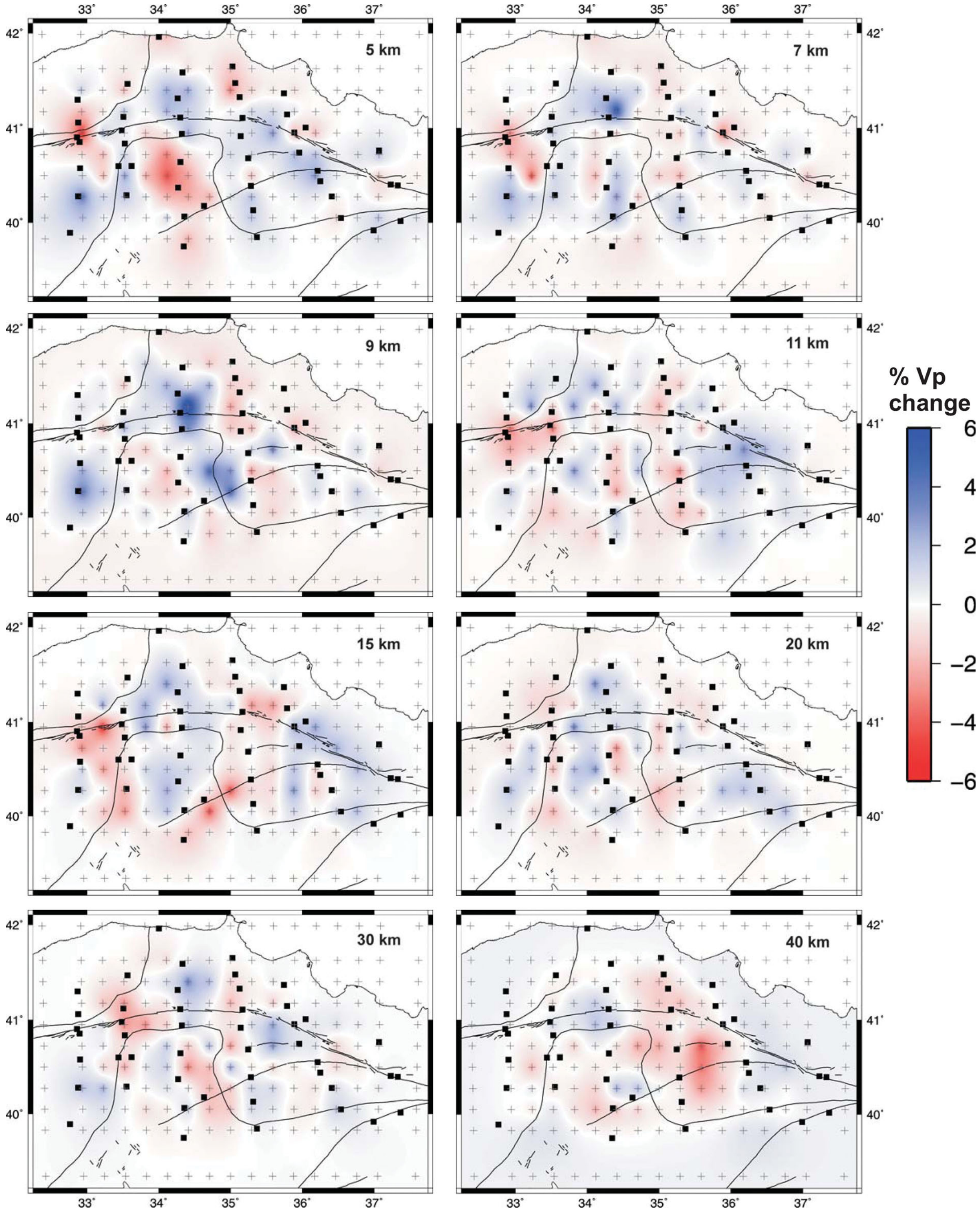

Figure 12. *P*-wave velocity perturbations (per cent) relative to the initial velocity model used in the inversion. Stations and grid nodes are shown by squares and plus signs, respectively. Black lines show major faults and sutures within the study area. See text for interpretation.

resolution is between 5 and 25 km depth, and hence these depths will be emphasized in the discussion. We have very little resolution in the upper 5 km, except directly beneath each station, and so shallow depths will not be discussed in any detail.

4.1 Relocated earthquakes

Throughout the study area, the distribution of earthquake focal depths indicates that the seismogenic zone is limited to the

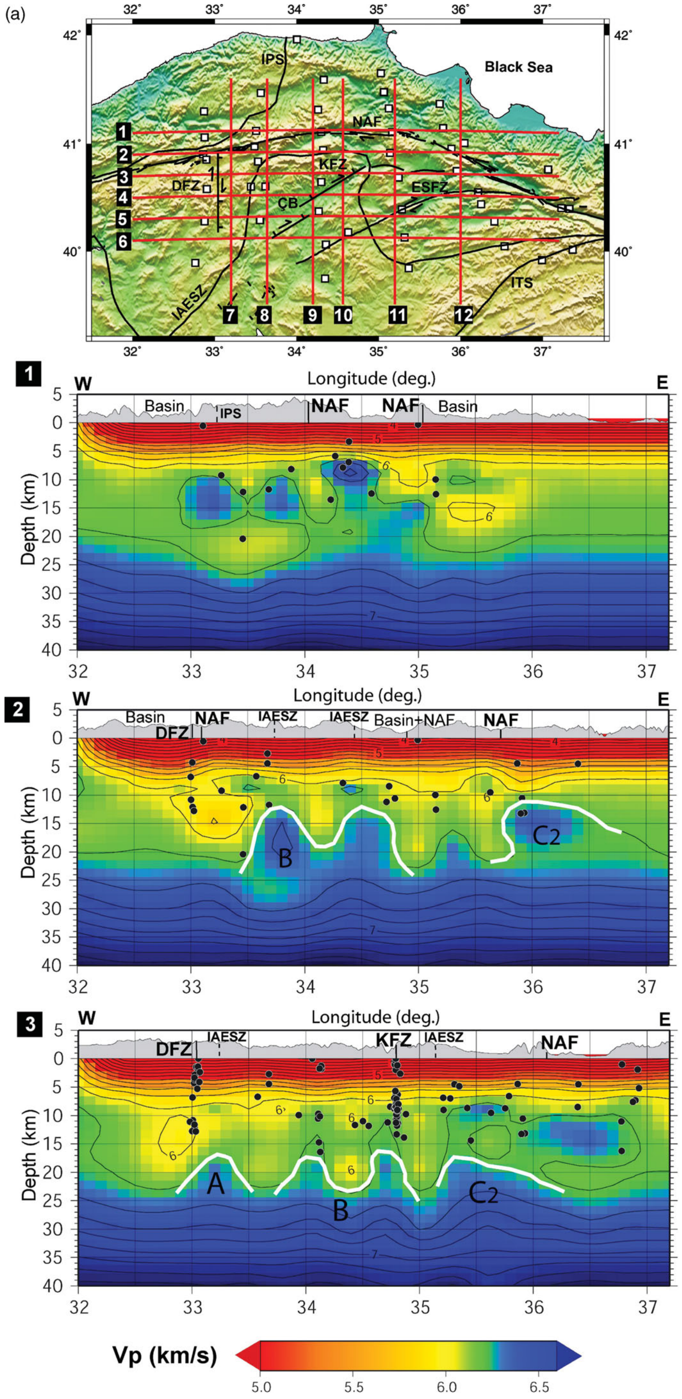

Figure 13 (a) E–W cross-sections through the final 3-D *P*-wave velocity model. The V_p velocities are colour coded and contoured every 0.2 km s^{-1}. Final earthquake hypocentres are projected onto the profiles as black circles. Topography with $2\times$ vertical exaggeration and main tectonic structures are given on top of each cross-section. A, B, C$_1$ and C$_2$ refer to the interpreted anomalies (continental fragments). DFZ, Dodurga Fault Zone; ÇB, Çankırı Basin; ESFZ, Ezine Pazarı-Sungurlu Fault Zone; IAESZ, İzmir-Ankara-Erzincan Suture; NAF, North Anatolian Fault; KFZ, Kızılırmak Fault Zone; IPS, Intra-Pontide Suture; ITS, Intra-Tauride Suture. (Faults and sutures are taken from Okay & Tüysüz 1999; Koçyiğit *et al.* 2001; Taymaz *et al.* 2007a,b; Kaymakçı *et al.* 2009, 2010). (b) E–W cross-sections through the final 3-D *P*-wave velocity model. The V_p velocities are colour coded and contoured every 0.2 km s^{-1}. Final earthquake hypocentres are projected onto the profiles as black circles. Topography with $2\times$ vertical exaggeration and main tectonic structures are given on top of each cross-section. A, B, C$_1$ and C$_2$ refer to the interpreted anomalies (continental fragments). DFZ, Dodurga Fault Zone; ÇB, Çankırı Basin; ESFZ, Ezine Pazarı-Sungurlu Fault Zone; IASZ, İzmir-Ankara-Erzincan Suture; NAF, North Anatolian Fault; KFZ, Kızılırmak Fault Zone; IPS, Intra-Pontide Suture; ITS, Intra-Tauride Suture (Faults and sutures are taken from Okay & Tüysüz 1999; Koçyiğit *et al.* 2001; Taymaz *et al.* 2007a,b; Kaymakçı *et al.* 2009, 2010). (c) N-S cross-sections through the final 3-D *P*-wave velocity model. The V_p velocities are colour coded and contoured every 0.2 km s^{-1}. Final earthquake hypocentres are projected onto the profiles as black circles. Topography with $2\times$ vertical exaggeration and main tectonic structures are given on top of each cross-section. A, B, C$_1$ and C$_2$ to the interpreted anomalies (continental fragments). DFZ, Dodurga Fault Zone; ÇB, Çankırı Basin; ESFZ, Ezine Pazarı-Sungurlu Fault Zone; IASZ; İzmir-Ankara-Erzincan Suture; NAF, North Anatolian Fault; KFZ, Kızılırmak Fault Zone; IPS, Intra-Pontide Suture; ITS, Intra-Tauride Suture (Faults and sutures are taken from Okay &Tüysüz 1999; Koçyiğit *et al.* 2001; Taymaz *et al.* 2007a,b; Kaymakçı *et al.* 2009, 2010).

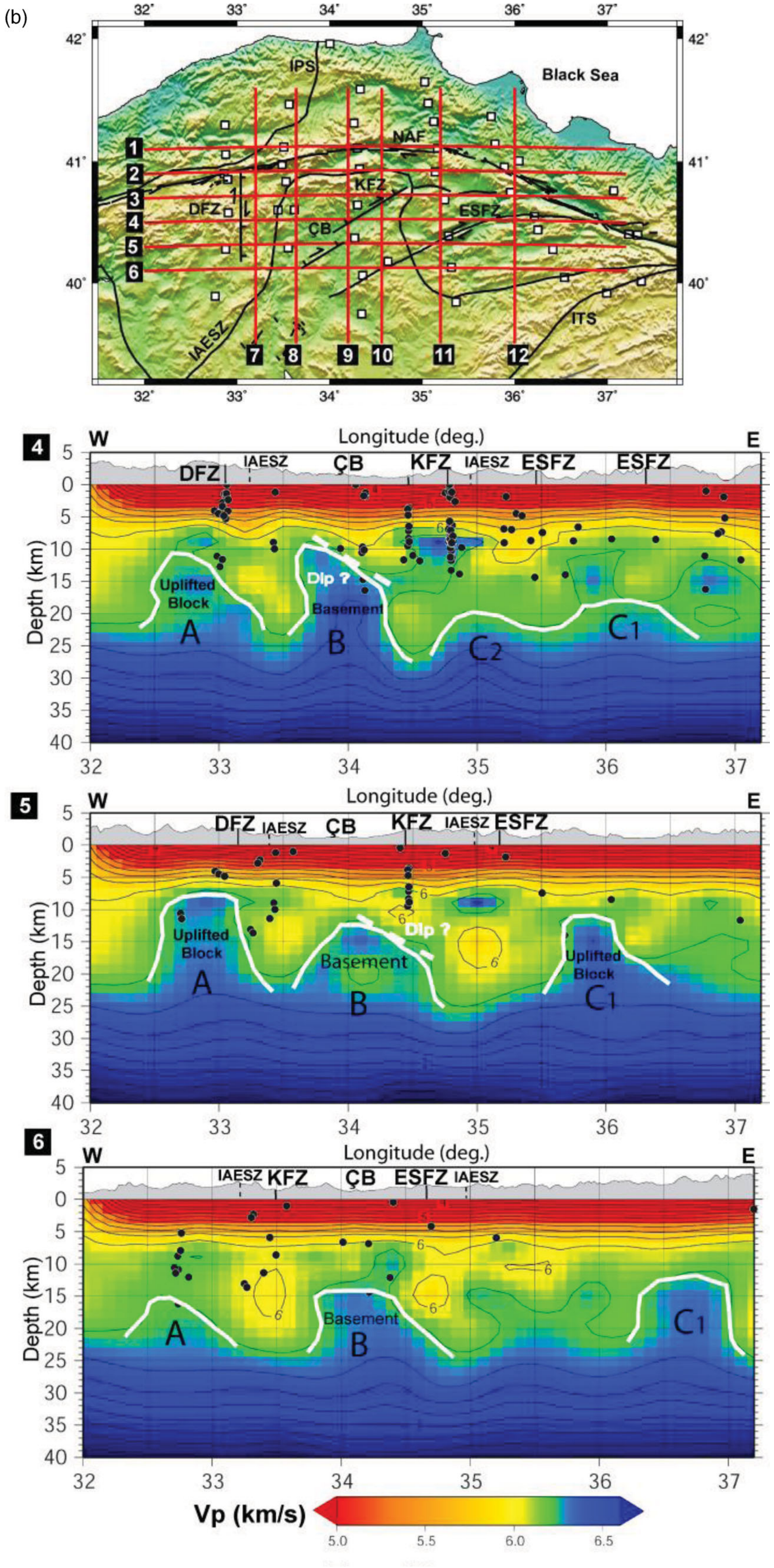

Figure 13. (*Continued.*)

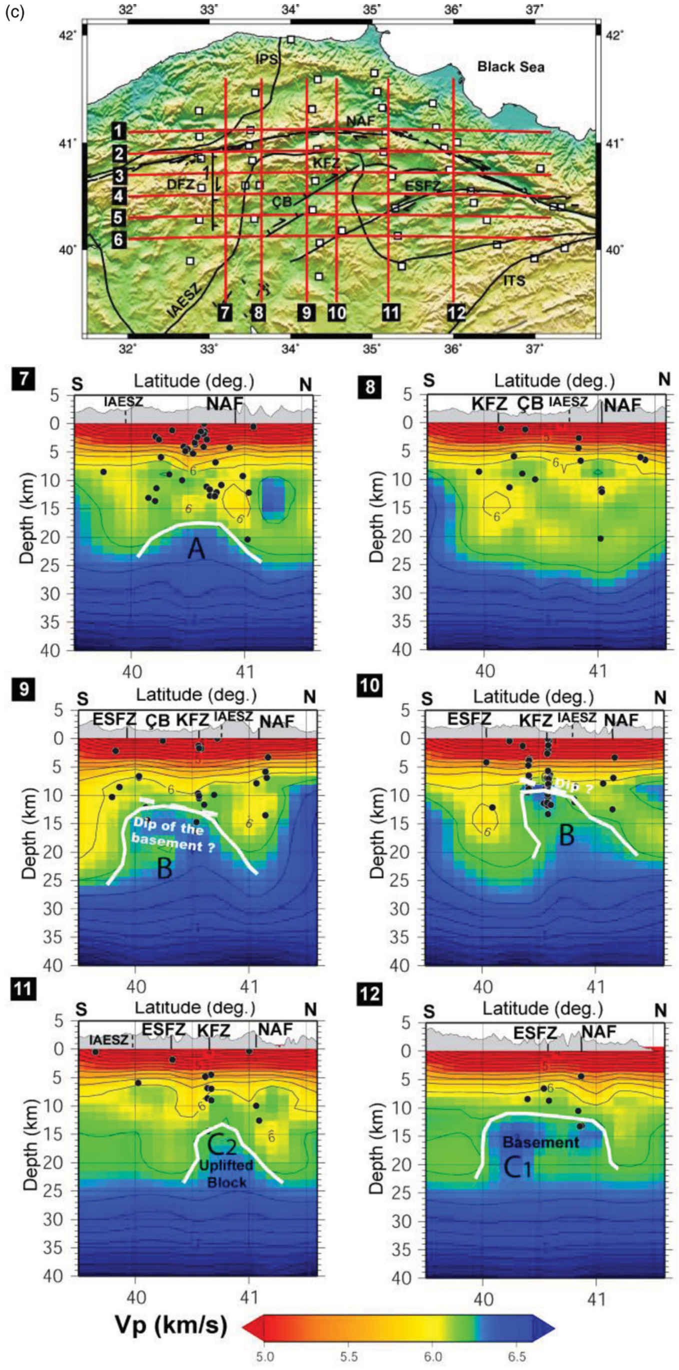

Figure 13. (*Continued.*)

upper 15 km of the north-central Anatolian crust (Fig. 11). The final earthquake locations obtained from the 3-D inversion are distributed throughout the study region, with most of these earthquakes occurring off of the NAF zone. According to our results, only 20 per cent of the 168 well-located earthquakes ($M \geq 3.0$) occurred along the NAFZ, with the remaining 80 per cent clustered along the various fault splays (Figs 13 and 14). Many of these earthquakes occur along the N–S striking Dodurga Fault Zone (DFZ, Fig. 1b). This fault is a left-lateral strike-slip fault with a normal component that bifurcates from the Çerkeş-Kurşunlu segment of the NAFZ around Çerkeş (Koçyiğit *et al.* 2001; Taymaz *et al.* 2007b). Taymaz *et al.* (2007b) emphasized that the DFZ is composed of a number of parallel to obliquely oriented faults with considerable amounts of normal slip component. A number of morphotectonic features in the region, related to strike-slip mechanisms such as pull-apart basins, alluvial fans and landslides, have been identified (see Koçyiğit *et al*. 2001; Taymaz *et al.* 2007b). Taymaz *et al*. (2007b) suggested this fault was the source of the 2000 June 6 Orta ($M_w \sim 6.0$) earthquake. In this study we recorded several aftershocks of this earthquake that occurred along the DFZ (Fig. 11). The swarm of small earthquakes located along this fault indicates that the fault is still very active, even 6–8 yr after the 2000 June 6 Orta main shock. Other

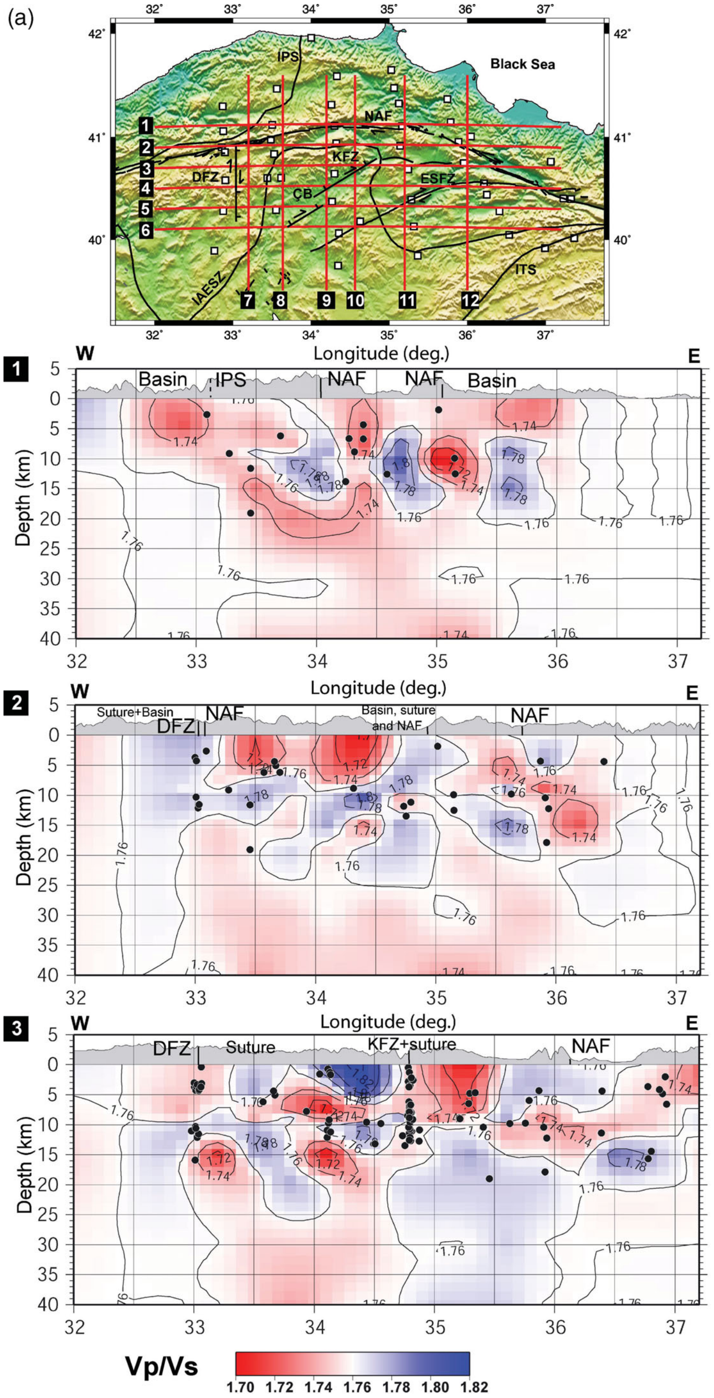

Figure 14 (a) E–W cross-sections through the final 3-D V_p/V_s ratio model. The V_p/V_s ratios are colour coded and contoured every 0.02. Final earthquake hypocentres obtained from the V_p/V_s inversion are projected onto the profiles as black circles. Topography with 2× vertical exaggeration and main tectonic structures are given on top of each cross-section. DFZ, Dodurga Fault Zone; ÇB, Çankırı Basin; ESFZ, Ezine Pazarı-Sungurlu Fault Zone; IAESZ, İzmir-Ankara-Erzincan Suture; NAF, North Anatolian Fault; KFZ, Kızılırmak Fault Zone; IPS, Intra-Pontide Suture; ITS, Intra-Tauride Suture (Faults and sutures are taken from Okay & Tüysüz 1999; Koçyiğit *et al.* 2001; Taymaz *et al.* 2007a,b; Kaymakçı *et al.* 2009, 2010). (b) E–W cross-sections through the final 3-D V_p/V_s ratio model. The V_p/V_s ratios are colour coded and contoured every 0.02. Final earthquake hypocentres obtained from the V_p/V_s inversion are projected onto the profiles as black circles. Topography with 2× vertical exaggeration and main tectonic structures are given on top of each cross-section. DFZ, Dodurga Fault Zone; ÇB, Çankırı Basin; ESFZ, Ezine Pazarı-Sungurlu Fault Zone; IAESZ, İzmir-Ankara-Erzincan Suture; NAF, North Anatolian Fault; KFZ, Kızılırmak Fault Zone; IPS, Intra-Pontide Suture; ITS, Intra-Tauride Suture (Faults and sutures are taken from Okay & Tüysüz 1999; Koçyiğit *et al.* 2001; Taymaz *et al.* 2007a,b; Kaymakçı *et al.* 2009, 2010). (c) N–S cross-sections through the final 3-D V_p/V_s ratio model. The V_p/V_s ratios are colour coded and contoured every 0.02. Final earthquake hypocentres obtained from the V_p/V_s inversion are projected onto the profiles as black circles. Topography with 2× vertical exaggeration and main tectonic structures are given on top of each cross-section. DFZ, Dodurga Fault Zone; ÇB, Çankırı Basin; ESFZ, Ezine Pazarı-Sungurlu Fault Zone; IAESZ, İzmir-Ankara-Erzincan Suture; NAF, North Anatolian Fault; KFZ, Kızılırmak Fault Zone; IPS, Intra-Pontide Suture; ITS, Intra-Tauride Suture (Faults and sutures are taken from Okay & Tüysüz 1999; Koçyiğit *et al.* 2001; Taymaz *et al.* 2007a,b; Kaymakçı *et al.* 2009, 2010).

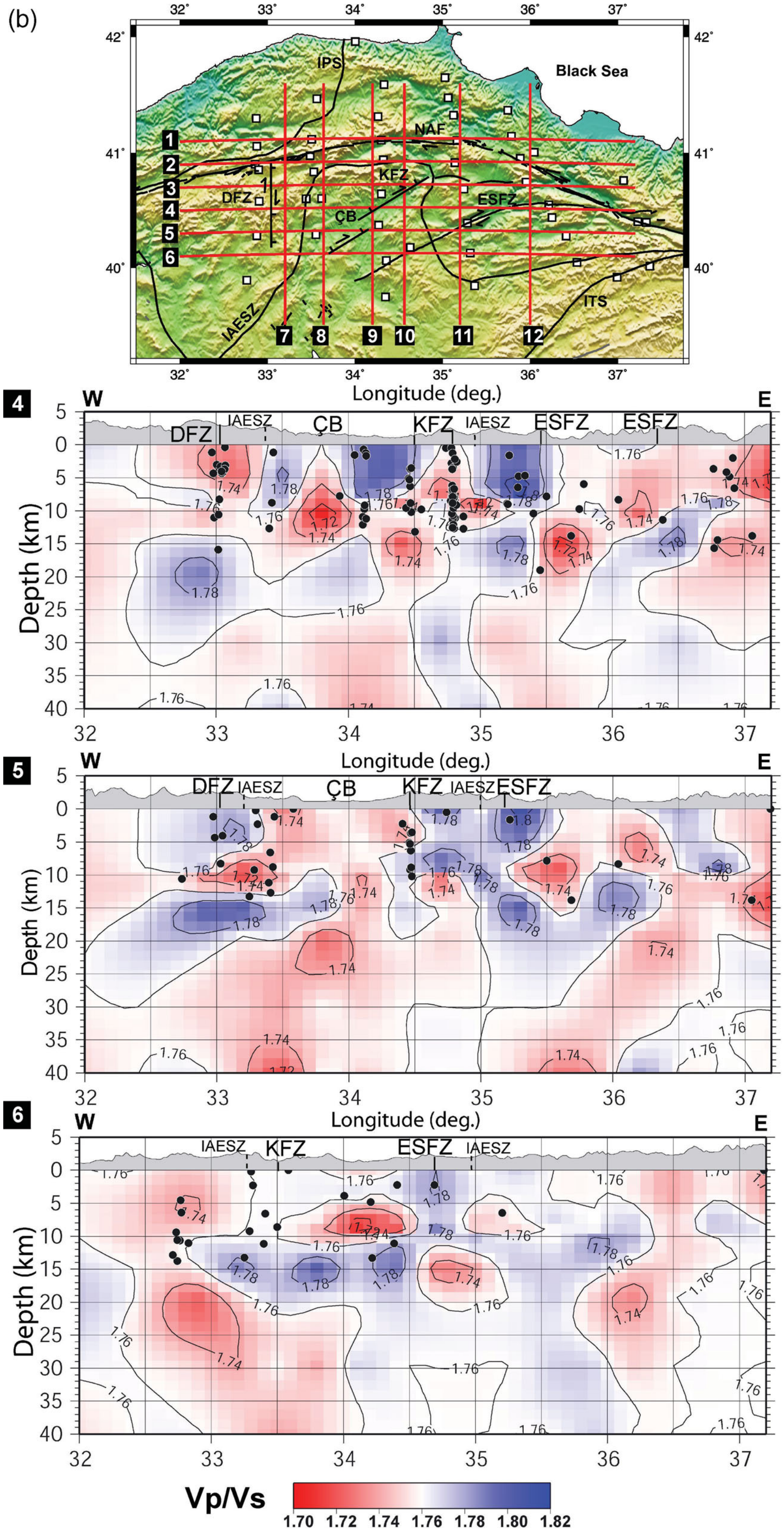

Figure 14. (*Continued.*)

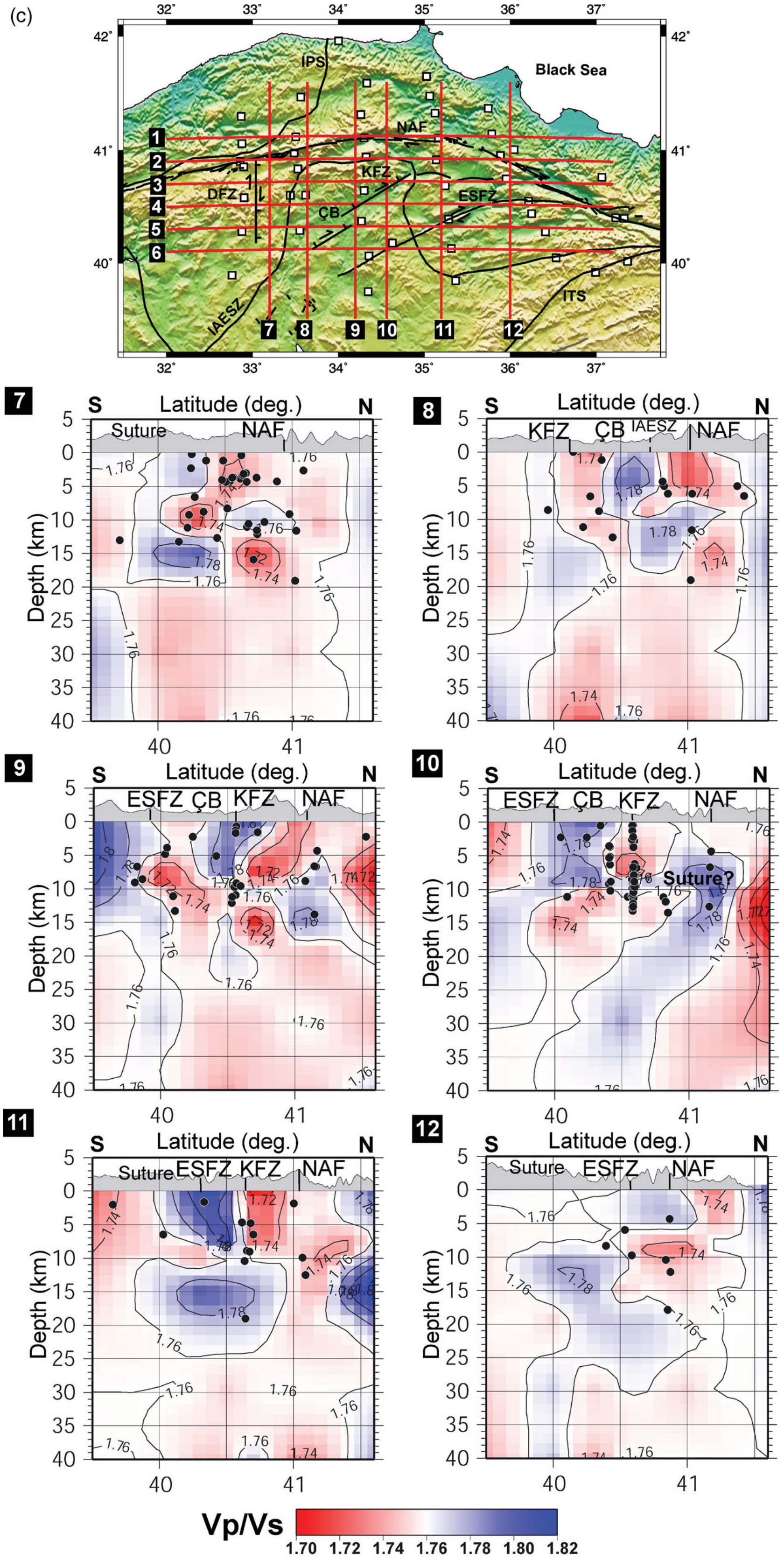

Figure 14. (*Continued.*)

prominent structures that control the seismicity in the region are the Kızılırmak (KFZ), Eldivan (EFZ), Laçin (LFZ) and Ezine Pazarı-Sungurlu Fault Zones (ESFZ) (Fig. 1b, Kaymakçı *et al.* 2003). These are major splays of the NAFZ within the study area, and the seismicity associated with them extends down to about 15 km depth in a linear fashion (Fig. 11), similar to the seismogenic depth of the DFZ.

The study region is associated with five major historical ($M >$ 6.5) destructive earthquakes along the NAFZ: the 1939, 1942, 1943, 1944 and 1951 earthquakes (McKenzie 1972; Barka 1996; Stein *et al.* 1997). The extents of the ruptures associated with these earthquakes are shown in Fig. 11. We cannot observe any clear correlation between the diffuse distribution of earthquake swarms and the extent of the historical ruptures along the fault. This lack of correlation and distributed seismicity along several segments of the NAFZ might be an indicator of an interseismic stage, where strain energy is accumulating along locked portions of the fault.

4.2 Crustal structure: *P*-wave velocity and V_p/V_s

The 3-D *P*-wave velocity structure and V_p/V_s variations are interpreted using a series of map slices and vertical cross-sections shown in Figs 12–14.

Our tomographic models show *P*-wave velocities from 5.4 to 6.5 km s^{-1} between 5 and 25 km in the crust. In the east–west cross-sections, the mid-crust shows large lateral variations in the *P*-wave speeds that are interpreted as variations in depth to basement blocks (Figs 13a and b). The *P*-wave velocity pattern is best seen in Fig. 15 with a map of the depth to the 6.2 km s^{-1} surface. At least three major blocks can be identified that bring higher velocity material to depths between 5 and 10 km, labelled as A, B, C1 and C2. The İzmir-Ankara-Erzincan Suture Zone appears to separate these blocks. Blocks A and C1 and C2 are north of the IAESZ, while block B is to the south. These blocks are interpreted as continental fragments that were accreted onto Eurasia as a result of continental collision following the terminal closure of the Neo-Tethys Ocean. According to Okay & Tüysüz (1999), the İzmir-Ankara-Erzincan Suture is generally indicated by post-Eocene thrusts that emplaced rocks of the Sakarya Continent to the north over the Tethyan subduction–accretion complexes to the south, forming a 5–10-km-wide tectonic belt. These high *P*-wave velocity ($\geq$6.2 km s^{-1}) blocks are thus considered to be continental basement fragments enclosed in lower velocity accretionary materials. Although the accretionary materials contain some oceanic lithosphere, including ophiolites, they are dominated by sedimentary materials of lower velocity (Okay & Tüysüz 1999).

The NAFZ cuts through a major high-velocity block to the east (anomalies C1, C2, Fig. 15) in the region where it has a transtensional character. However, it is located between blocks in the central and western parts, where it is more transpressional (Fig. 15). Much of the NAFZ is associated with relatively low *P*-wave velocities between 5 and 15 km depth (Fig. 13). Most of the fault splays such as the ESFZ and the KFZ appear to rupture through the high-velocity blocks and may represent new faults that are controlled by pre-existing structures in the mid-crust.

The western end of the 1939 earthquake rupture zone terminates at the edge of block C1. This high-velocity region may have served as a barrier to the 1939 earthquake, as the rupture appears to have veered off the main trace of the NAFZ where it intersects the high-velocity block. The 1942 earthquake appears to have ruptured a small part of this block with high-velocity material at shallow depths. The 1943 earthquake initiated at the edge of block C1 and continued rupturing along the edge of block C2, into the bend containing low-velocity material (Fig. 15).

In addition, we observe very low *P*-wave velocity anomalies (V_p $\sim$4.0–5.0 km s^{-1}) in the Çankırı Basin, located in the central part of the region, and several other smaller basins at shallower depths ($<$5 km; i.e. Ulus, Çerkeş-Kurşunlu, Merzifon and Havza; Figs 12 and 13). We note, however, that this anomaly is at the edge of our shallow depth resolution. The Çankırı Basin is composed of a 5-km-thick sedimentary sequence (Kaymakçı *et al.* 2003), that spatially correlates with a region of low *P*-wave velocity obtained from our inversion, extending to a depth of $\sim$8–10 km. The base of this region of low *P*-wave velocity is clearly seen in the cross-section near 40.5°N (Fig. 13c, profile 9) at a depth of 10–15 km. Kaymakçı *et al.* (2003) reported that the granitoids of the Kırşehir Block delimit the southern margin of the basin and constitute the basement. In agreement with the observations of Kaymakçı *et al.* (2003) and Okay & Tüysüz (1999), we suggest that this basement dips northwards in the central part of the region and crops out outside of the study area to the south (see Figs 13a–c). Thus the crystalline core of the basement of the Çankırı Basin is characterized by relatively higher *P*-wave velocities (V_p $\sim$6.2 km s^{-1}) than its surrounding region and descends down to about 10–12 km depth (see Profiles 5 and 9 in Figs 13b and c).

We find large variations in the V_p/V_s ratio in the mid-crust in the study area (Fig. 14). The V_p/V_s ratio can be an indication of the mechanical and petrological properties of the crust (Roecker 1982; Eberhart-Phillips 1990; Thurber 1993). It can also be interpreted as an indicator of lithology and/or fractures, cracks and pore spaces in the upper crust (Tatham 1982). It is commonly reported that the high V_p/V_s zones indicate fluid-rich regions. For example, Wu *et al.* (2007) observed high V_p/V_s values along the sutures and volcanic arc belts in Taiwan. Zhao & Negishi (1998) also found low V_p and high V_p/V_s at the source zone of the 1995 Kobe earthquake, and concluded that these anomalies were related to the fluid-filled, fractured rock matrix at the source and contributed to the initiation of the Kobe earthquake. Vanorio *et al.* (2005) proposed that low V_p/V_s values characterize rocks with empty or gas-filled fractures. Based on an LET study along the eastern part of NAFZ, Kaypak (2008) reported low V_p/V_s values and associated these anomalies with the fractured, gas-filled and very porous rocks along small segments of the NAFZ within strike-slip sedimentary basins at shallow depths (0–4 km). Results presented here indicate the Çankırı Basin deposits are characterized by low *P*-wave velocity and high V_p/V_s, possibly reflecting water-saturated sediments at shallow depths ($<$8 km) (Figs 13 and 14). Although the correlation is not perfect, in general the areas of shallow basement contain low V_p/V_s, and areas of thicker accretionary materials have high V_p/V_s. This is consistent with the more felsic composition of continental blocks (i.e. the basement of Çankırı Basin) and the high V_p/V_s of more mafic accretionary materials. Also, zones of fluids are more likely to be found within fractured, intensively deformed accretionary materials, resulting in observations of high V_p/V_s (Fig. 14).

The NAFZ is associated with regions of both high and low V_p/V_s. In some parts of the study area, the upper 6–8 km appear to have low V_p/V_s, transitioning to high V_p/V_s ratios between 8 and 15 km depth (Fig. 14c, profiles 7–9). Some profiles show a broad region of low V_p/V_s in the vicinity of the NAFZ (Fig. 14c, profile 11), while others show higher V_p/V_s ratios (Fig. 14c, profile 10). Based on these observations, the segments of NAFZ with low V_p/V_s regions at depth

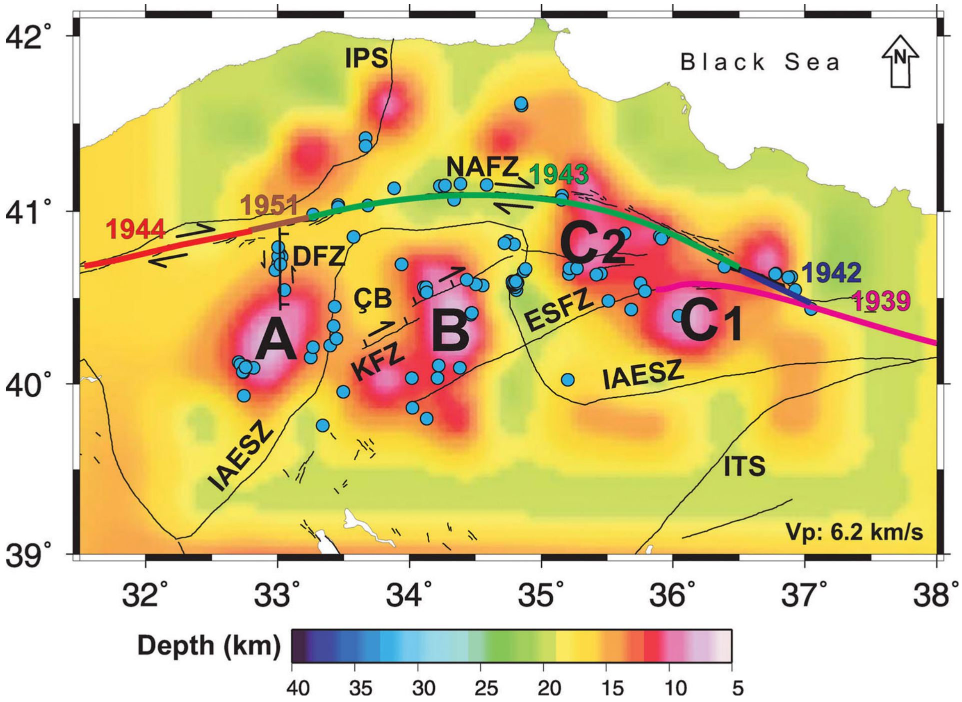

Figure 15. Summary map of the depth to the $V_p = 6.2$ km s^{-1} surface, with rupture extents of the historical 1939, 1942, 1943, 1944 and 1951 earthquakes (McKenzie 1972; Barka 1996; Stein *et al.* 1997). Colour scale indicates the depth to the *P*-wave velocity anomaly. The higher velocity blocks that extend into shallow regions of the mid-crust are shown in pink and the lower velocity regions, where the 6.2 km s^{-1} surface is deeper, are shown in green. Only earthquakes in the depth range of the mapped surface are plotted. A, B, C$_1$ and C$_2$ refers the continental fragments that were accreted onto Eurasia as a result of continental collision following the terminal closure of the Neo-Tethys Ocean. IAESZ, Izmir-Ankara-Erzincan Suture Zone; DFZ, Dodurga Fault Zone; ESFZ, Ezine Pazarı–Sungurlu Fault Zone; ÇB, Çankırı Basin; KFZ, Kızılırmak Fault Zone; NAFZ, North Anatolian Fault Zone; IPS, Intra-Pontide Suture; ITS, Intra-Tauride Suture.

might be associated with shear zones that have lower fluid contents compared to the segments associated with high V_p/V_s values. We interpret the variation of anomalous V_p/V_s values along the NAFZ to be related to the variable fluid content of the shear zones (Janssen *et al.* 1997). The ESFZ, a splay of the NAFZ, has high V_p/V_s ratios, as shown in Fig. 14(b) (profiles 4–6) and Fig. 14(c) (profiles 10 and 11), which may also reflect high fluid content along this fault.

5 CONCLUSIONS

Using earthquakes recorded by the combination of a passive seismic experiment along the NAFZ and the national permanent KOERI stations, the 3-D *P*-wave velocity structure and the V_p/V_s variations from ∼5 km to 30 km depth were imaged in north-central Anatolia. The detailed analysis of the solution quality, checkerboard tests and resolution estimates reveals good resolution for this depth range, especially in the central part of the study area.

Our analysis indicates the lower limit of the seismogenic zone for north-central Anatolia is located at 15 km depth. Final earthquake locations display a distributed pattern throughout the study area, with most of the earthquakes occurring on the major splays of NAFZ (i.e. KFZ, ESFZ and DFZ), rather than its master strand. The scarcity of earthquakes along the central part of the North Anatolian Fault suggests that this portion of the fault is in a general, interseismic locked stage following the destructive 1939, 1942, 1943, 1944 and 1951 earthquakes.

We identified three major high-velocity blocks, each separated by the IAESZ. These blocks are interpreted to be continental basement fragments that influenced the rupture extents of the historical 1939, 1942 and 1943 earthquakes. The top of the central block identifies the basement of the Çankırı Basin (∼8–10 km depth). These continental basement fragments are associated with low V_p/V_s ratios, possibly due to their felsic composition. In contrast, the regions associated with accretionary materials have higher V_p/V_s ratios, suggesting they contain more fluids and/or have an overall more mafic composition. Large variations in V_p/V_s anomalies in the study area might be related to variations in the fluid content of existing lithologies and their related structures.

ACKNOWLEDGMENTS

This study was funded by İstanbul Technical University Research Fund (İTÜ-BAP), Turkish National Scientific and Technological Foundation (TÜBİTAK), International Postdoctoral Research Scholarship Program (TÜBİTAK-BIDEP), Turkish Academy of Sciences (TÜBA) in the framework for Young Scientist Award Program (TT – TÜBA – GEBIP 2001), and it was partially supported by US-NSF grant EAR0309838. We also thank the Kandilli Observatory and Earthquake Research Institute (KOERI) for providing us the additional local earthquake data. Generic Mapping Tools (GMT; Wessel & Smith 1998) and IRIS-ANTELOPE commercial software suite from BRTT (1998) were used to prepare figures and to process earthquake data, respectively. Special thanks to Christine R. Gans, Stephen Husen and Ivonne Arroyo for their help and support in using the LET codes. The authors thank Christine R. Gans and Gökhan Çevikbilen for helpful discussions, suggestions and enthusiastic support. Careful reviews by two anonymous referees resulted in considerable improvement to an earlier version of this manuscript. We are particularly indebted to Editor-In-Chief Jeannot Trampert for his judicious insightful remarks.

REFERENCES

Adıyaman, O., Chorowicz, J., Arnaud, O.N., Gündoğdu, M.N. & Gourgaud, A., 2001. Late Cenozoic tectonics and volcanism along the North Anatolian Fault: new structural and geochemical data, *Tectonophysics*, **338**, 135–165.

Ambraseys, N.N., 2002. The seismic activity of the Marmara Sea region over the last 2000 years, *Bull. seism. Soc. Am.*, **92**, 1–18.

Armijo, R., Meyer B., Barka, A.A. & Hubert, A., 1999. Propagation of the North Anatolian fault into the Northern Aegean: timing and kinematics, *Geology*, **27**, 267–270.

Arroyo, I.G., Husen, S., Flueh, E.R., Gossler, J., Kissling, E. & Alvarado, G.E., 2009. Three-dimensional P-wave velocity structure on the shallow part of the Central Costa Rican Pacific margin from local earthquake tomography using off- and onshore networks, *Geophys. J. Int*, **179**, doi:10.1111/j.1365-246X.2009.04342.x.

Ateş, A., Kearey, P. & Tufan, S., 1999. New gravity and magnetic anomaly maps of Turkey, *Geophys. J. Int.*, **136**, 499–502.

Atwater, T., 1970. Implications of plate tectonics for the Cenozoic tectonic evolution of western North America, *Geol. Soc. Am. Bull.*, **81**(12), 3513–3536.

Barka, A., 1996. Slip distribution along the North Anatolian Fault associated with the large earthquakes of the period 1939 to 1967, *Bull. seism. Soc. Am.*, **86**, 1238–1254.

Barka, A., Akyüz, H.S., Cohen, H.A. & Watchorn, F., 2000. Tectonic evolution of the Niksar and Tasova–Erbaa pull-apart basins, North Anatolian Fault Zone: their significance for the motion of the Anatolian block, *Tectonophysics*, **322**, 243–264.

Barış, S., Nakajima, J., Hasegawa, A., Honkura, Y., Ito, A. & Üçer, S.B., 2005. Three dimensional structure of Vp, Vs and Vp/Vs in the upper crust of the Marmara region, NW Turkey, *Earth Planets Space*, **57**(11), 1019–1038.

Bécel, A., Laigle, M., de Voogd, B., Hirn, A., Taymaz, T., Yolsal-Cevikbilen, S. & Shimamura, H., 2010. North Marmara Trough architecture of basin infill, basement and faults, from PSDM reflection and OBS refraction seismics, *Tectonophysics*, **490**, 1–14.

Biryol, C.B., Zandt, G., Beck, S.L., Özacar, A.A., Adıyaman, H.E. & Gans, C., 2010. Shear wave splitting along a nascent plate boundary: the North Anatolian Fault Zone, *Geophys. J. Int.*, **181**, 1201–1213, doi:10.1111/j.1365-246X.2010.04576.x

Bozkurt, E. & Koçyiğit, A., 1996. The Kazova basin: an active negative flower structure on the Almus Fault Zone, a splay fault system of the North Anatolian Fault Zone, Turkey, *Tectonophysics*, **265**, 238–254.

BRTT, 1998. *Antelope Installation and Operations Manual: Documentation for Antelope Environmental Monitoring Software, Software Release 4.1*, Boulder Real-Time Technologies, Inc., Boulder, 38 p.

Çakır, Ö. & Erduran, M., 2011. On the P and S receiver functions used for inverting the one-dimensional upper mantle shear-wave velocities, *Surv. Geophys.*, **32**, 71–98.

Dewey, J.F., Hempton, M.R., Kidd, W.S.F., Saroglu, F. & Şengör, A.M.C., 1986. Shortening of continental lithosphere: the tectonics of Eastern Anatolia—young collision zone, in collision tectonics, *Spec. Publ. Geol. Soc. London*, **19**, 3–36.

Dias, N.A.L. Matias, N., Lourenço, J., Madeira, F., Carrilho, J. L. & Gaspar, J.L., 2007. Crustal seismic velocity structure near Faial and Pico Islands (AZORES), from local earthquake tomography, *Tectonophysics*, **445**, 301–317, doi:10.1016/j.tecto.2007.09.001.

Dickinson, W.R. & Wernicke, B.P., 1997. Reconciliation of San Andreas slip discrepancy by a combination of interior basin and range extension and transrotation near the coast, *Geology*, **25**, 663–665.

Douglas, A., 1967. Joint epicenter determination, *Nature*, **215**, 47–48.

Eberhart-Phillips, D., 1986. Three-dimensional velocity structure in Northern California Coast Ranges from inversion of local earthquake arrival times, *Bull. seism. Soc. Am.*, **76**, 1025–1052.

Eberhart-Phillips, D., 1990. Three-dimensional P and S velocity structure in the Coalinga region, California, *J. geophys. Res.*, **95**, 15 343–15 363.

Eberhart-Phillips, D., 1993. Local earthquake tomography: earthquake source regions, in *Seismic Tomography: Theory and Practice*, pp. 613–643, eds Iyer, H.M. & Hiahara, K., Chapman and Hall, London.

Eberhart-Phillips, D. & Reyner, M., 1997. Continental subduction and three dimensional crustal structure: the northern South Island, New Zealand, *J. geophys. Res.*, **102**, 11 843–11 861.

Evans, J.R., Eberhart-Phillips, D. & Thurber, C.H., 1994. User's manual for SIMULPS12 for imaging *Vp* and *Vp*/*Vs*: a derivative of the Thurber tomographic inversion SIMUL3 for local earthquakes and explosions, *U.S. Geol. Surv. Open-File Report*, U.S. Government Printing Office, 94–431.

Gans, C.R., Beck, S., Zandt, G., Biryol, C.B. & Özacar, A.A., 2009. Detecting the limit of slab break-off in central Turkey: new high resolution P_n tomography results, *Geophys. J. Int.*, **179**, 1566–1572.

GEBCO-BODC, 1997. *General Bathymetric Chart of the Oceans,* British Oceanographic Data Centre, Birkenhead, CD-ROM.

Görür, N., Oktay, F.Y., Seymen, İ. & Şengör, A.M.C., 1984. Palaeotectonic evolution of the Tuzgölü basin complex, Central Turkey: sedimentary record of a Neotethyan closure, *Geol. Soc. London Spec. Pub.,* **17,** 467–482, doi:10.1144/GSL.SP.1984.017.01.34.

Görür, N., Tüysüz, O. & Şengör, A.M.C., 1998. Tectonic evolution of the Central Anatolia Basin, *Int. Geol. Rev.*, **40**, 831–850.

Gürbüz, C., Bekler, T., Toksoz, M.N., Kuleli, S., Kalafat, D. & Schultz, C.A., 2003. Seismic refraction studies and crustal structure in Anatolia. Commission on controlled-source seismology: deep seismic methods, in *12th International Workshop, Mountain Lake*, 8–11 October 2003, Virginia, USA.

Haberland, C., Rietbrock, A., Lange, D., Bataille, K. & Dahm, T., 2009. Structure of the seismogenic zone of the southcentral Chilean margin revealed by local earthquake traveltime tomography, *J. geophys. Res.*, **114**, doi:10.1029/2009JB005802.

Haslinger, F. & Kissling, E., 2001. Investigating effects of 3-D ray tracing methods in local earthquake tomography, *Phys. Earth planet. Int.*, **123**, 103–114.

Haslinger, F. *et al*., 1999. 3D crustal structure from local earthquake tomography around Gulf of Arta (Ionian region), NW Greece, *Tectonophysics*, **304**, 210–218.

Hodgson, J.H. & Wickens, A.J., 1965. Computer-determined P-nodal solutions for the larger earthquakes of 1959–1962, *Publ. Dom. Obs., Ottawa*, **31**, 123–143.

Hubert-Ferrari, A., King, G., Van Der Woerd, J., Villa, I., Altunel, E. & Armijo, R., 2009. Long-term evolution of the North Anatolian Fault: new constraints from its eastern termination, *Geol. Soc. London Spec. Pub.,* **311,** 133–154, doi:10.1144/SP311.5.

Husen, S., Kissling, E. & Flueh, E., 2000. Local earthquake tomography of shallow subduction in North Chile: a combined onshore and offshore study, *J. geophys. Res.*, **105**, 28 183–28 198.

Husen, S., Quintero, R., Kissling, E. & Hacker, B., 2003. Subduction-zone structure and magmatic processes beneath Costa Rica constrained by local earthquake tomography and petrological modeling, *Geophys. J. Int.*, **155**, 11–32.

Husen, S., Smith, R.B. & Waite, G.P., 2004. Evidence for gas and magmatic sources beneath the Yellowstone volcanic field from seismic tomography imaging, *J. Volc. Geotherm. Res.*, **131**, 397–410.

Janssen, C., Michel, G.W., Bau, M., Lüders, V. & Mühle, K., 1997. The North Anatolian Fault Zone and the role of fluids in seismogenic deformation, *J. Geol.*, **105**, 387–403.

Karabulut, H., Özalaybey, S., Taymaz, T., Aktar, M., Selvi, O. & Kocaoğlu, A., 2003. A tomographic image of the shallow crustal structure in the Eastern Marmara, *Geophys. Res. Lett.*, **30**(24), doi: 10.1029/2003GL018074.

Kaymakçı, N., 2000. Tectono-stratigraphical evolution of the Cankırı Basin (Central Anatolia, Turkey), *PhD thesis,* Geologica Ultraiectina. No. 190, Utrecht University, ISBN 90-5744-047-4.

Kaymakçı, N., White, S.H. & Van Dijk P.M., 2003. Kinematic and structural development of the Çankırı Basin (Central Anatolia, Turkey). A paleostress inversion study, *Tectonophysics*, **364**, 85–113.

Kaymakçı, N., Özçelik, Y., White, S.H. & Van Dijk, P.M., 2009. Tectonostratigraphy of the Çankırı Basin: Late Cretaceous to early Miocene evolution of the Neotethyan Suture Zone in Turkey, *Geol. Soc. London Spec. Pub.,* **311,** 67–106, doi:10.1144/SP311.3.

Kaymakçı, N., Özmutlu, Ş., Van Dijk, P.M. & Özçelik, Y., 2010. Surface and subsurface characteristics of the Çankırı Basin (Central Anatolia, Turkey): integration of remote sensing, seismic interpretation and gravity, *Turk. J. Earth Sci.*, **19**, 79–100.

Kaypak, B., 2008. Three-dimensional Vp and Vp/Vs structure of the upper crust in the Erzincan basin (eastern Turkey), *J. geophys. Res.*, **113**, doi:10.1029/2006JB004905.

Ketin, I., 1966. Tectonic units of Anatolia, *Bull. Miner. Res. Explor. Inst. Ankara*, **66**, 23–34.

Kissling, E., 1988. Geotomography with local earthquakes, *Rev. Geophys.*, **26**, 659–698.

Kissling, E., Ellsworth, W.L., Eberhart-Phillips, D. & Kradolfer, U., 1994. Initial reference models in local earthquake tomography, *J. geophys. Res.*, **99**, 19 635–19 646.

Kissling, E., Kradolfer, U. & Maurer, H., 1995. *VELEST User's Guide: Short Introduction*, Institute of Geophysics and Swiss Seismological Service, ETH, Zurich.

Kissling, E., Husen, S. & Haslinger, F., 2001. Model parameterization in seismic tomography: a choice of consequences for the solution quality, *Phys. Earth planet. Inter.*, **123**, 89–101.

Koçyiğit, A., 1991. An example of an accretionary forearc basin from northern Central Anatolia and its implications for the history of subduction of Neo-Tethys in Turkey, *Geol. Soc. Am. Bull.*, **103**, 22–36.

Koçyiğit, A. & Beyhan, A., 1998. A new intrcontinental transcurrent structure: the Central Anatolian Fault Zone, *Tectonophysics*, **284**, 317–386.

Koçyiğit, A., Rojay, B., Cihan, M. & Özacar, A., 2001. The June 6, 2000, Orta (Çankırı, Turkey) earthquake: sourced from a new antithetic sinistral strike-slip structure of the North Anatolian Fault System, the Dodurga Fault Zone, *Turk. J. Earth Sci.*, **10**, 69–82.

Koulakov, I. *et al*., 2007. P and S velocity structure of the crust and the upper mantle beneath central Java from local tomography inversion, *J. geophys. Res.*, **112**, doi:10.1029/2006JB004712.

Koulakov, I., Bindi, D., Parolai, S., Grosser, H. & Milkereit, C., 2010. Distribution of seismic velocities and attenuation in the crust beneath the north Anatolian Fault (Turkey) from local earthquake tomography, *Bull. seism. Soc. Am.*, **100**(1), 207–224, doi:10.1785/0120090105.

Kuleli, S., Toksoz, M., Gurbuz, C., Gok, R. & Schultz, C., 2004. Crustal structure study in Turkey with controlled seismic sources, *EOS, Trans. Am. geophys. Un.,* **85**(47), Fall Meet. Suppl., Abstract S13B-1058.

McClusky, S. *et al*., 2000. Global positioning system constraints on plate kinematics and dynamics in the eastern Mediterranean and Caucasus, *J. geophys. Res.*, **105**, 5695–5719, doi:10.1029/1999JB900351.

McClusky, S., Reilinger, R., Mahmoud, S., Ben Sari, D. & Tealeb, A., 2003. GPS constraints on Africa (Nubia) and Arabia plate motion, *Geophys. J. Int.*, **155**, 126–138.

McKenzie, D., 1972. Active tectonics of Mediterranean region, *Geophys. J. R. astr. Soc.*, **30**, 109–185.

McKenzie, D.P. & Morgan, W.J., 1969. Evolution of triple junctions, *Nature*, **224**, 125–133.

Nakamura, A. *et al*., 2002. P-wave velocity structure of the crust and its relationship to the occurrence of the 1999 Izmit, Turkey earthquake and aftershocks, *Bull. seism. Soc. Am.*, **92**, 330–338.

Okay, A. & Tüysüz, O., 1999. Tethyan sutures of northern Turkey, *Geol. Soc. London Spec. Pub.,* **156,** 475–515, doi:10.1144/GSL.SP.1999.156.01.22.

Öcal, N., 1966. Geometrical solutions of fault plane problem of the destructive earthquakes occurred in Anatolia in the period 1938–1955, *Z. Geophys. J.*, **32**, 293–309.

Paul, A., Cattaneo, M., Thouvenot, F., Spallarossa, D., Bethoux, N. & Frechet, J., 2001. A three-dimensional crustal velocity model of the southwestern Alps from local earthquake tomography, *J. geophys. Res.*, **106**, 19 367–19 389.

Piper, J.D.A., Moore, J., Tatar, O., Gürsoy H. & Park, R.G., 1996. Palaeomagnetic study of crustal deformation across an intra-continental transform: the North Anatolian Fault Zone in Northern Turkey, *Geol. Soc. London Spec. Pub.,* **105,** 299–310, doi:10.1144/GSL.SP.1996.105.01.26.

Pujol, J., 1988. Comments on the joint determination of hypocenters and station corrections, *Bull. seism. Soc. Am.*, **78**, 1179–1189.

Robertson, A.H.F., Parlak, O. & Ustaömer, T., 2009. Melange genesis and ophiolite emplacement related to subduction of the northern margin of the Tauride-Anatolide continent, central and western Turkey, *Geol. Soc. London Spec. Pub.,* **311,** 9–66, doi:10.1144/SP311.2.

Roecker, S.W., 1982. The velocity structure of the Pamir-Hindu Kush region: possible evidence of subducted crust, *J. geophys. Res.*, **87**, 945–959.

Rowlands, D.P., White, R.S. & Haines, A. J., 2005. Seismic tomography of the Tongariro Volcanic Centre, New Zealand, *Geophys. J. Int.*, **163**, 1180–1194.

Salah, M.K., Şahin, S. & Kaplan, M., 2007. Seismic velocity structure along the western segment of the North Anatolian Fault Zone imaged by seismic tomography, *Bull. Earthq. Res. Inst. Univ. Tokyo,* **82**, 209–223.

Saunders, P., Priestly, K. & Taymaz, T., 1998. Variations in the crustal structure beneath western Turkey, *Geophys. J. Int.*, **134**, 373–389.

Searcy, C.K., 2003. Station corrections for the Katmai region seismic network, USGS Open-File Report, USA.

Seyitoğlu, G. *et al*., 2009. A late pliocene – quaternary pinched crustal wedge in NW Central Anatolia, Turkey: a neotectonic structure accommodating the internal deformation of the Anatolian Plate, *Geol. Bull. Turkey*, **52**(1), 121–154.

Smith, W.H.F. & Sandwell, D.T., 1997a. *Measured and Estimated Seafloor Topography* (version 4.2). World Data Centre A for Marine Geology and Geophysics Research, Publication RP-1, poster.

Smith, W.H.F. & Sandwell, D.T., 1997b. Global seafloor topography from satellite altimetry and ship depth soundings, *Science*, **277**, 1957–1962.

Stein, R.S., Barka, A.A. & Dieterich, J.H., 1997. Progressive failure on the North Anatolian fault since 1939 by earthquake stress triggering, *Geophys. J. Int.*, **128**, 594–604.

Şaroğlu, F., Emre, Ö. & Kuşçu, İ., 1992. *Active Fault Map of Turkey*, 2 sheets, MTA, Ankara-Turkey.

Şengör, A.M.C., 1979. North Anatolian Fault: its age, offset and tectonic significance, *J. geol. Soc. Lond.*, **136**, 269–282.

Şengör, A.M.C., Görür, N. & Şaroğlu, F., 1985. Strike-slip faulting and related basin formation in zones of tectonic escape: Turkey as a case study, in strike-slip faulting and basin formation, *Spec. Publ. Soc. Econ. Paleontol. Mineral.* **37**, 227–264.

Şengör, A.M.C., Tüysüz O., İmren, C., Sakınç, M., Eyidoğan, H., Görür, N., Le Pichon, X. & Rangin, C., 2005. The North Anatolian Fault: a new look, *Annu. Rev. Earth planet. Sci.*, **33,** 37–112, doi:10.1146/annurev.earth.32.101802.120415.

Tatar, O., Piper, J.D.A., Gürsoy, H. & Temiz, H., 1996. Regional significance of Neotectonic counterclockwise rotation in Central Turkey, *Int. Geol. Rev.*, **38**, 692–700.

Tatham, R.H., 1982. Vp/Vs and lithology, *Geophysics*, **47**, 336–344.

Taymaz, T., 1996. S-P-wave traveltime residuals from earthquakes and lateral inhomogeneity in the upper mantle beneath Aegean and the Hellenic Trench near Crete, *Geophys. J. Int.*, **127**(2), 545–558.

Taymaz, T. 1999. Seismotectonics of the Marmara Region: Source Characteristics of 1999 Gölcük-Sapanca Düzce Earthquakes, in *Proceedings of ITU-IAHS, International Conference On The Kocaeli Earthquake*, Istanbul, Turkey, 1999 August 17, pp. 55–78.

Taymaz, T., Jackson, J. & McKenzie, D., 1991. Active Tectonics of the North and Central Aegean Sea, *Geophys. J. Int.*, **106**(2), 433–490.

Taymaz, T., Westaway, R. & Reilinger, R., 2004. Active faulting and crustal deformation in the Eastern Mediterranean Region, *Tectonophysics*, **391**(1–4), 1–9.

Taymaz, T., Yılmaz, Y. & Dilek, Y., 2007a. The Geodynamics of the Aegean and Anatolia: Introduction, *Geol. Soc. London Spec. Pub.,* **291,** 1–16, doi:10.1144/SP291.1.

Taymaz, T., Wright, T., Yolsal, S., Tan, O., Fielding, E. & Seyitoğlu, G., 2007b. Source characteristics of June 6, 2000 Orta-Çankırı (Central Turkey) Earthquake: a synthesis of seismological, geological and geodetic (InSAR) observations, and internal deformation of Anatolia Plate, *Geol. Soc. London Spec. Pub.,* **291,** 259–290, doi:10.1144/SP291.12.

Thurber, C.H., 1981. Earth structure and earthquake locations in the Coyote Lake area, central California, *PhD thesis,* MIT, Cambridge, MA, 331 pp.

Thurber, C.H., 1992. Hypocenter-velocity structure coupling in local earthquake tomography, *Phys. Earth planet. Inter.*, **75**, 55–62.

Thurber, C.H., 1993. Local earthquake tomography: velocities and Vp/Vs:: theory, in *Seismic Tomography: Theory and Practice*, pp. 563–583, Chapman and Hall, London.

Thurber, C.H. & Eberhart-Phillips, D., 1999. Local earthquake tomography with flexible gridding, *Comput. Geosci.*, **25**, 809–818, doi:10.1016/S0098-3004(99)00007-2.

Thurber, C., Roecker, S., Ellsworth, W., Chen, Y., Lutter, W. & Sessions, R., 1997. Two dimensional seismic image of the San Andreas Fault in the Northern Gabilan Range, Central California: evidence for fluids in the fault zone, *Geophys. Res. Lett.*, **24**, 1591–1594.

Thurber, C., Zhang, H., Brocher, T. & Langenheim, V., 2009. Regional three dimensional seismic velocity model of the crust and uppermost mantle of northern California, *J. geophys. Res.*, **114**, doi:10.1029/2008JB005766.

Tok, H.E., Beck, S.L, Zandt, G., Biryol, C.B., Warren, L.M., Özacar, A.A. & Taymaz, T., 2008. NAF experiment: lithospheric structure of the central north Anatolia from S-wave receiver function analysis, *EOS, Trans. Am. geophys. Un.,* **89**(53), Fall Meet. Suppl., Abstract T21A-1917.

Toksöz, M.N., Kuleli, S., Gurbüz, C., Kalafat, D., Bekler, T., Zor, E., Yılmazer, M., Ogutcu, Z., Schulta, C.A. & Harris, D.B., 2003. Calibration of regional seismic stations in the Middle East with shots in Turkey, in *Proceedings of the 25th Seismic Research Review Mtg.*, NNSA/AFRL, Tucson, AZ.

Trampert, J. & Spetzler, J., 2006. Surface wave tomography: finite-frequency effects lost in the null space, *Geophys. J. Int.*, **164**, 394–400.

Van der Meijde, M., van der Lee, S. & Giardini, D., 2003. Crustal structure beneath broad-band seismic stations in the Mediterranean region, *Geophys. J. Int.*, **152**(3), 729–739.

Vanoria, T., Virieux, J., Capuano, P. & Russo, G., 2005. Three-dimensional seismic tomography from P wave and S wave microearthquake travel times and rock physics characterization of the Campi Flegrei Caldera, *J. geophys. Res.*, **110**, doi:10.1029/2004JB003102.

Virieux, J. & Farra, V., 1991. Ray tracing in 3-D complex isotropic media: an analysis of the problem, *Geophysics*, **56**, 2057–2069.

Wessel, P. & Smith, W.H.F., 1998. New version of the Generic Mapping Tools Released. *EOS, Trans. Am. geophys. Un.*, **79**(47), 579.

Westaway, R., 1994. Present-day kinematics of the Middle East and Eastern Mediterranean, *J. geophys. Res.*, **99**, 12 071–12 090.

Wu, Y.-M., Chang, C-H., Zhao, L., Shyu, B.H., Chen, Y.-G., Sieh, K. & Avouac, J-P., 2007. Seismic tomography of Taiwan: improved constraints from a dense network of strong motion stations, *J. geophys. Res.*, **112**, doi:10.1029/2007JB004983.

Yolsal, S., 2008. Source mechanism parameters and slip distributions of Crete-Cyprus Arcs, dead sea transform fault earthquakes and historical tsunami simulations, *PhD thesis,* Istanbul Technical University.

Yolsal, S. & Taymaz, T., 2010. Sensitivity analysis on relations between earthquake source rupture parameters and far-field tsunami waves: case studies in the eastern Mediterranean region, *Turk. J. Earth Sci.*, **19**, 313–349.

Yolsal, S., Taymaz, T. & Yalçıner, A.C., 2007. Understanding tsunamis, potential source regions and tsunami prone mechanisms in the Eastern Mediterranean, *Geol. Soc. London Spec. Pub.,* **291,** 201–230, doi:10.1144/SP291.10.

Zhao, D. & Negishi, H., 1998. The 1995 Kobe earthquake: seismic image of the source zone and its implications for the rupture nucleation, *J. geophys. Res.*, **103**, 9967–9986.

APPENDIX A: JACKKNIFE TESTS

To evaluate the dependence of the results on any particular earthquakes in the data set, a jackknife test was performed by randomly discarding 10 earthquakes in each of 17 inversion runs. Standard deviations of the velocities and the mean velocities (Figs A1 and A2) were calculated for each gridpoint in each model layer for all of the 17 jackknife tests. Gridpoints are found where the velocities are robustly below or above the reference model when the standard deviation for that particular gridpoint is added or subtracted (Fig. A3). More precisely, the robust nodes and associated jackknife values are found according to the relational algorithm developed by Van der Meijde *et al.* (2003).

Thus the non-robust values/grid cells are masked on these plots and only the robust regions and values are shown. These plots show that the well-sampled central regions generally yield robust results for all performed jackknife tests (see Fig. A3), also indicated by very low values of standard deviations shown on maps of standard deviations for each layer (Fig. A1). In addition, the cross-section along ∼40.5°N (line 4 on Fig. 13a), which samples most of the interpreted anomalies in the region, shows small variations for individual tests and suggests that these anomalies are resolved (Figs A4 and A5). There are small variations in the amplitude of the anomalies, especially for anomalies C1 and C2.

Layer thickness test

An alternative model parametrization containing much thicker layers (–5 km, 0 km, 10 km, 20 km, 30 km and 40 km), was tested. The best damping parameter for this new parametrization was determined, and a checkerboard test was calculated. The results of this test indicate that the major anomalies A and B interpreted in this study are still observable, but anomaly C1 is quite variable. (Fig. A6). In the inversion with thicker layers, anomaly C1 has a lower V_p than in this study (containing thinner layers).

APPENDIX B: SOURCE PARAMETERS OF MAJOR EARTHQUAKES

Source mechanisms of major earthquakes ($M > 6.0$) occurred along the NAFZ are summarized in Table B1.

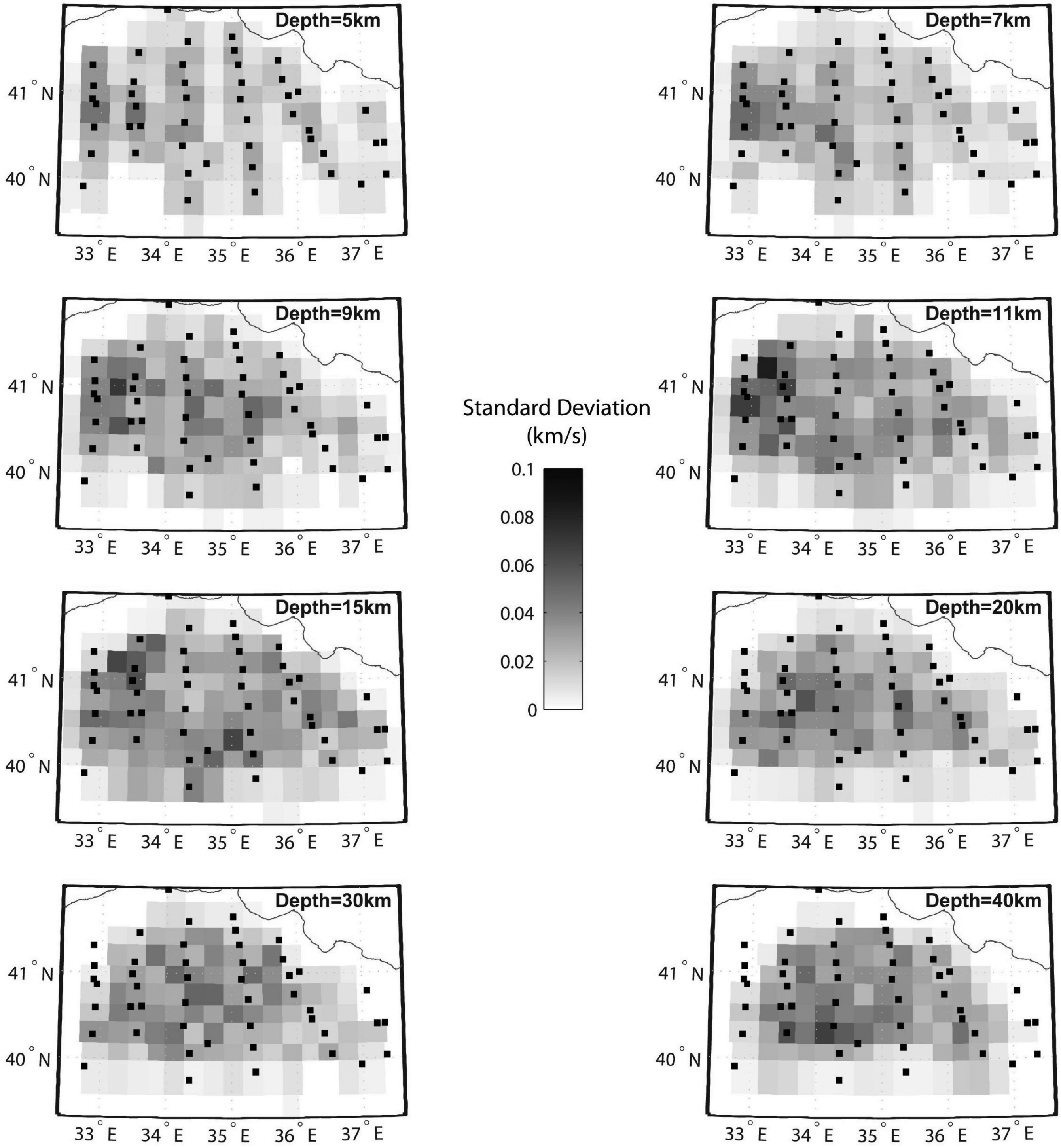

Figure A1. Standard deviation (σ) values of velocities for each gridpoint in each model layer for all of the 17 jackknife tests.

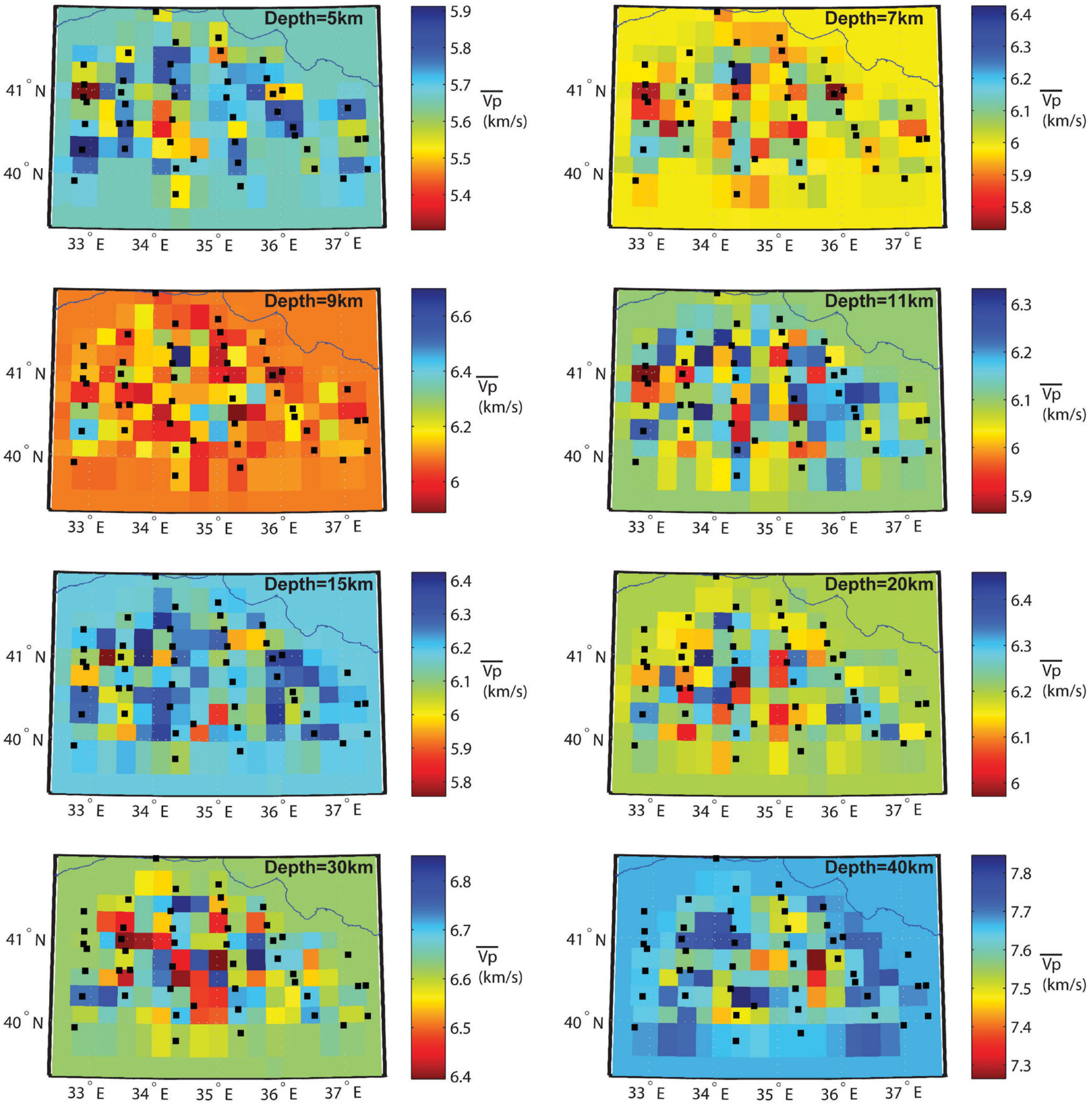

Figure A2. Mean velocities calculated for each gridpoint in each model layer for all of the 17 jackknife tests.

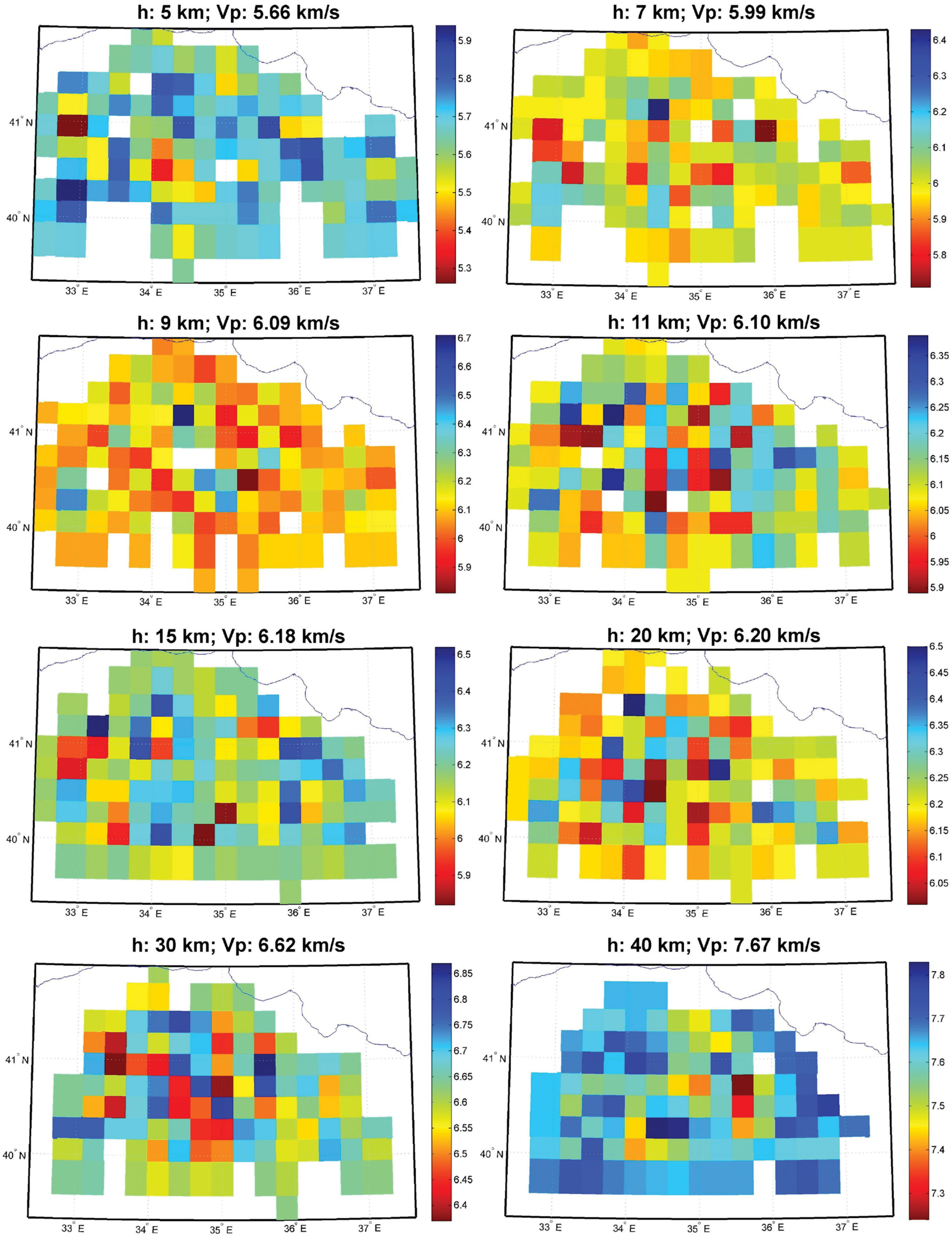

h: 5 km; Vp: 5.66 km/s

h: 7 km; Vp: 5.99 km/s

h: 9 km; Vp: 6.09 km/s

h: 11 km; Vp: 6.10 km/s

h: 15 km; Vp: 6.18 km/s

h: 20 km; Vp: 6.20 km/s

h: 30 km; Vp: 6.62 km/s

h: 40 km; Vp: 7.67 km/s

Figure A3. Calculated robust nodes acquired from jackknife test results. Above the maps, layer depth and related *P*-wave velocities are given. Coloured scales show *P*-wave velocities.

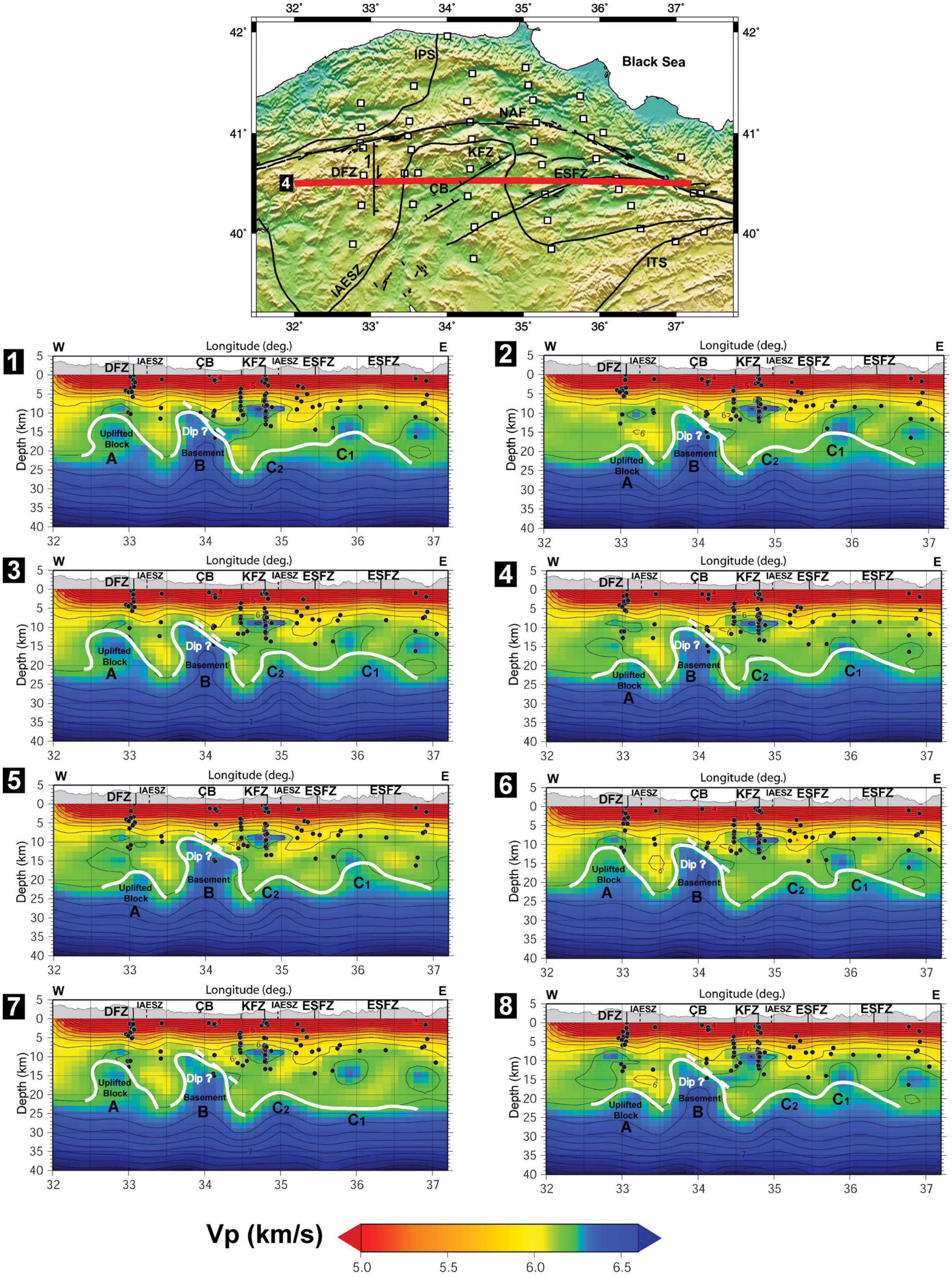

Figure A4. E–W cross-sections along profile 4 (latitude ~40.5°) through the 3-D *P*-wave velocity models obtained from different jackknife tests (1–8). The V_p velocities are colour coded and contoured every 0.2 km s^{-1}. Final earthquake hypocentres are projected onto the profiles as black circles. Topography with 2× vertical exaggeration and main tectonic structures are given on top of each cross-section. A, B, C_1 and C_2 refer to the anomalies interpreted in this study DFZ, Dodurga Fault Zone; ÇB, Çankırı Basin; ESFZ, Ezine Pazarı-Sungurlu Fault Zone; IASZ, İzmir-Ankara-Erzincan Suture; NAF, North Anatolian Fault; KFZ, Kızılırmak Fault Zone; IPS, Intra-Pontide Suture; ITS, Intra-Tauride Suture (Faults and sutures are taken from Okay & Tüysüz 1999; Koçyiğit *et al.* 2001; Taymaz *et al.* 2007a,b; Kaymakçı *et al.* 2009, 2010).

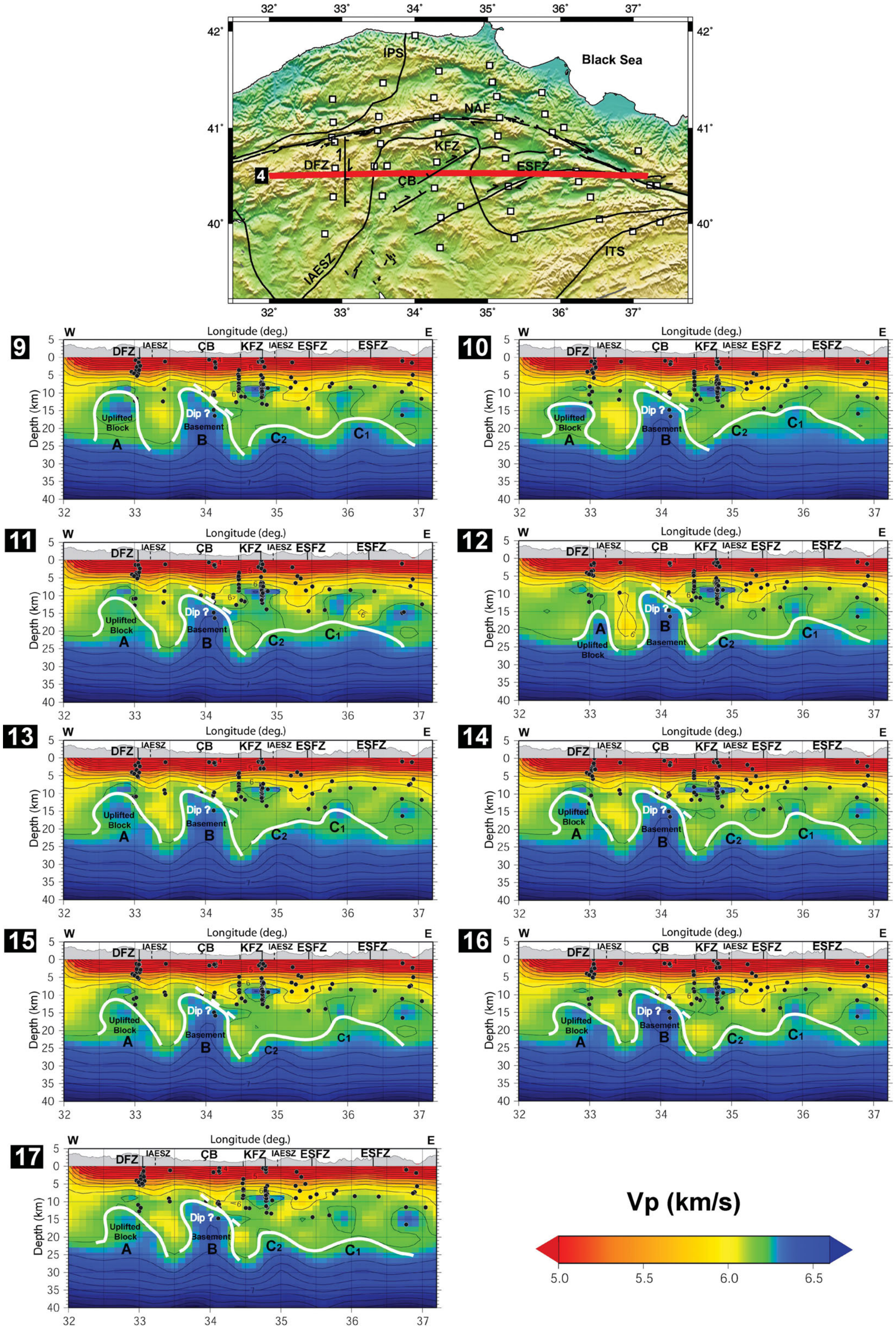

Figure A5. E–W cross-sections along profile 4 (latitude ∼40.5°) through the 3-D *P*-wave velocity models obtained from different jackknife tests (9–17). The V_p velocities are colour coded and contoured every 0.2 km s^{-1}. Final earthquake hypocentres are projected onto the profiles as black circles. Topography with 2× vertical exaggeration and main tectonic structures are given on top of each cross-section. A, B, C_1 and C_2 refer to the anomalies interpreted in this study as continental fragments that were accreted onto Eurasia as a result of continental collision following the terminal closure of the Neo-Tethys Ocean. DFZ, Dodurga Fault Zone; ÇB, Çankırı Basin; ESFZ, Ezine Pazarı-Sungurlu Fault Zone; IASZ, İzmir-Ankara-Erzincan Suture; NAF, North Anatolian Fault; KFZ, Kızılırmak Fault Zone; IPS, Intra-Pontide Suture; ITS, Intra-Tauride Suture (Faults and sutures are taken from Okay & Tüysüz 1999; Koçyiğit *et al.* 2001; Taymaz *et al.* 2007a,b; Kaymakçı *et al.* 2009, 2010).

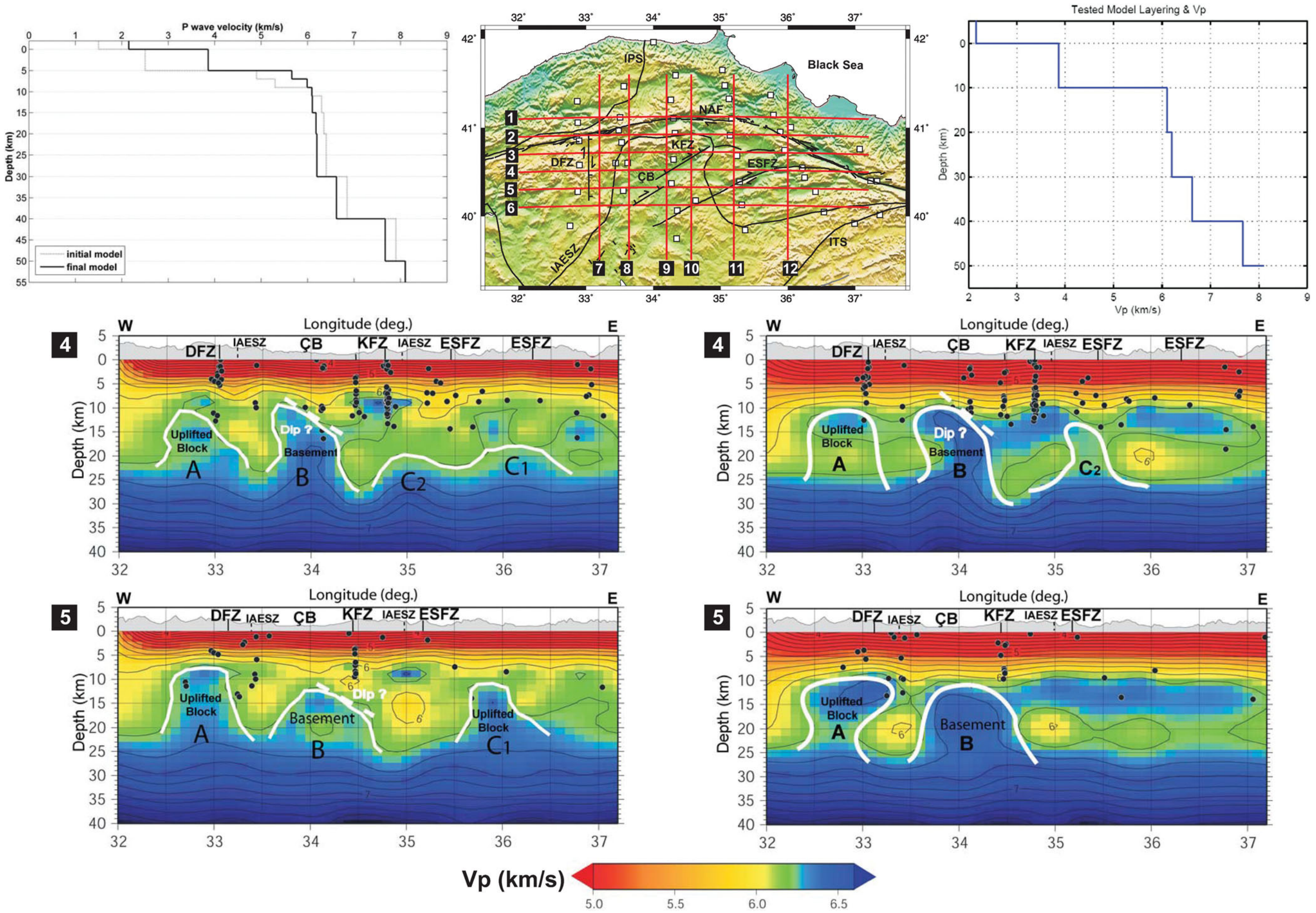

Figure A6. Comparison of P-wave tomography models using two different layer thickness parametrizations in the inversion. Upper left and right P-wave velocity models show starting 1-D thin-layers velocity model (left-hand side) and a thicker layer (right-hand side) velocity model used to compare the effects of different layer thickness. The resultant tomography in cross-sections along profiles 4 and 5 are shown below each velocity model. The V_p velocities are colour coded and contoured every 0.2 km s^{-1}. Final earthquake hypocentres are projected onto the profiles as black circles. Topography with 2× vertical exaggeration and main tectonic structures are given on top of each cross-section. A, B, C_1 and C_2 refer to the anomalies we interpreted in this study. Although there are some differences, in general anomalies A and B are robust for different layer thicknesses but the shapes of anomalies C1 and C2 are more sensitive to the layer thickness. DFZ, Dodurga Fault Zone; ÇB, Çankırı Basin; ESFZ, Ezine Pazarı-Sungurlu Fault Zone; IASZ, İzmir-Ankara-Erzincan Suture; NAF, North Anatolian Fault; KFZ, Kızılırmak Fault Zone; IPS, Intra-Pontide Suture; ITS, Intra-Tauride Suture (Faults and sutures are taken from Okay & Tüysüz 1999; Koçyiğit *et al.* 2001; Taymaz *et al.* 2007a,b; Kaymakçı *et al.* 2009, 2010).

Table B1. Source mechanism parameters of major earthquakes ($M > 6.0$) shown in Fig. 2(a). M, Magnitude; Lat, Latitude (°N); Lon, Longitude (°E); h, focal depth (km) and M_o, seismic moment (N m). Mc72, McKenzie (1972); O66, Öcal (1966); HW65, Hodgson & Wickens (1965); T91, Taymaz *et al.* (1991); T99, Taymaz (1999) and T07b, Taymaz et al. (2007b).

Date (dd.mm.yy)	Origin time (hh:mm)	Mag.	Lat. (°N)	Lon. (°E)	Strike (°)	Dip (°)	Rake (°)	h (km)	M_o (10^{16} N m)	Ref.
26.12.1939	23:57	7.8	39.80	39.38	108	86	151	-	-	Mc72
20.12.1942	14:03	7.1	40.66	36.35	128	71	–176	-	-	066
26.11.1943	22:20	7.3	40.97	33.22	269	73	173	-	-	HW65
01.02.1944	03:22	7.3	41.10	33.20	332	77	31	-	-	066
13.08.1951	18:33	6.9	40.86	32.68	81	70	–172	-	-	Mc72
22.07.1967	16:56	7.1	30.69	40.67	275	88	–178	12	-	T91
27.03.1975	05:15	6.6	26.12	40.45	68	55	–145	15	200	T91
17.08.1999	00:01	7.7	40.76	29.96	92	89	–177	9	12000	T99
12.11.1999	16:57	7.4	40.81	31.19	276	59	–167	14	4500	T99
06.06.2000	02:41	6.0	40.65	32.92	2	46	–29	8	130	T07b